
SYMBOLIC REGRESSION OF DATA-DRIVEN REDUCED ORDER MODEL CLOSURES FOR UNDER-RESOLVED, CONVECTION-DOMINATED FLOWS

Simone Manti¹, Ping-Hsuan Tsai², Alessandro Lucantonio¹, Traian Iliescu²

¹Aarhus University, Katrinebjergvej 89G-F, 8000, Aarhus, Denmark

²Department of Mathematics, Virginia Tech, 225 Stanger Street, Blacksburg, 24061, VA, USA

ABSTRACT

Data-driven closures correct the standard reduced order models (ROMs) to increase their accuracy in under-resolved, convection-dominated flows. There are two types of data-driven ROM closures in current use: (i) structural, with simple ansatzes (e.g., linear or quadratic); and (ii) machine learning-based, with neural network ansatzes. We propose a novel symbolic regression (SR) data-driven ROM closure strategy, which combines the advantages of current approaches and eliminates their drawbacks. As a result, the new data-driven SR closures yield ROMs that are interpretable, parsimonious, accurate, generalizable, and robust. To compare the data-driven SR-ROM closures with the structural and machine learning-based ROM closures, we consider the data-driven variational multiscale ROM framework and two under-resolved, convection-dominated test problems: the flow past a cylinder and the lid-driven cavity flow at Reynolds numbers $Re = 10000, 15000, \text{ and } 20000$. This numerical investigation shows that the new data-driven SR-ROM closures yield more accurate and robust ROMs than the structural and machine learning ROM closures.

Keywords Reduced order modeling, symbolic regression, convection-dominated flows, data-driven closure, machine learning

1 Introduction

High-performance computing and modern numerical algorithms have made high-fidelity fluid-thermal analysis tractable in geometries of ever increasing complexity. Despite continued advances in these areas, direct numerical (DNS), large eddy simulation (LES), and even unsteady Reynolds-averaged Navier–Stokes (URANS) simulations of turbulent thermal transport remain too costly for routine analysis and design of thermal–hydraulic systems, where hundreds of cases must be considered.

Reduced order models (ROMs) offer a promising alternative by leveraging expensive high-fidelity simulations (referred to as full order models or FOMs) to first extract a low-dimensional basis that captures the principal features of the underlying flow fields, and then construct computational models whose dimensions are orders of magnitude lower than the FOM dimension. In the numerical simulation of fluid flows, Galerkin ROMs (G-ROMs), which use data-driven basis functions in a Galerkin framework, have provided efficient and accurate approximations of laminar flows, such as the two-dimensional flow past a circular cylinder at low Reynolds numbers [1, 2]. However, turbulent flows are notoriously hard for the standard G-ROM. Indeed, to capture the complex dynamics, a large number [3] of ROM basis functions is required, which yields high-dimensional ROMs that cannot be used in realistic applications. Thus, computationally efficient, low-dimensional ROMs are used instead. Unfortunately, these ROMs are inaccurate since the ROM basis functions that were not used to build the G-ROM have an important role in dissipating the energy from the system [4]. Indeed, without enough dissipation, the low-dimensional G-ROM generally yields spurious numerical

Corresponding author: a.lucantonio@mpe.au.dk (Alessandro Lucantonio)

oscillations. Thus, closures and stabilization strategies are required for the low-dimensional G-ROMs to be stable and accurate [4, 5, 6, 7, 8, 9].

The ROM closures are ROM corrections in which the standard G-ROM is supplemented with a ROM closure model, τ^{ROM} , which models the effect of the unresolved scales (i.e., the effect of the ROM basis functions that were not used to build the G-ROM). There are several types of ROM closure modeling strategies, which are carefully reviewed in [4].

Arguably the most popular class of ROM closures is data-driven ROM closures [4, 10], in which FOM data are used to train the ROM closure model. There are several data-driven approaches for modeling τ^{ROM} , which are surveyed in [4]. To construct the data-driven ROM closure model, τ^{ROM} , we first postulate a model form for τ^{ROM} . Currently, there are two strategies for the ROM closure model form:

1. A principled, structural strategy, in which the ROM closure model ansatz has a simple mathematical structure (e.g., a linear model or a quadratic model [11, 12]).
2. A nonintrusive, machine learning (ML) strategy, in which the ROM closure model ansatz is based on neural networks [4, 10, 13, 14].

In the final step of the construction of the data-driven ROM closure model, we leverage the available data to determine the unknown parameters in the ROM closure model ansatz. This can be achieved, e.g., by solving a least squares problem (for the structural strategy) or by minimizing a loss function (for the machine learning strategy).

Each strategy has pros and cons:

1. The structural strategy yields simple, interpretable ROM closure models, which can be easily combined with the ROM operators in the standard G-ROM. However, it is not clear that the simple building blocks (e.g., the linear and quadratic terms) can accurately represent the complex dynamics modeled by the ROM closure terms.
2. The machine learning strategy, on the other hand, yields models that can, in principle, approximate the complex underlying dynamics. However, this strategy yields ROM closure models that contain parameters whose meaning is generally unclear.

Finding data-driven ROM closure models that are both accurate and physically interpretable is a major challenge in the development of ROMs for realistic turbulent flows. In this paper, we propose a novel data-driven ROM closure modeling strategy that centers around symbolic regression (SR). The novel SR-ROM closure modeling strategy combines the advantages of the current approaches and eliminates their drawbacks: The SR-ROM closure models are interpretable, parsimonious (i.e., contain much fewer parameters than, e.g., the machine learning strategy), and are rich enough to approximate the complex ROM closure dynamics. Given the limited number of parameters that characterize the new SR-ROM closures, they are less prone to overfitting and, thus, generalize better than the current data-driven ROM closures. Furthermore, the new SR-ROM closure models have the following additional advantages: They are accurate, computationally efficient, and, because they are constructed by using a sound mathematical strategy, they are amenable to analysis. We emphasize that, although SR has been successfully used in data-driven modeling, to our knowledge, the SR-ROM closure model proposed in this paper is the first instance in which SR is used in ROM closure modeling.

To illustrate our new SR-ROM closure modeling strategy, we need to choose a data-driven ROM closure modeling approach. To this end, we choose the data-driven variational multiscale ROM (d2-VMS-ROM) [11, 12], which is a successful data-driven ROM closure modeling approach utilized in various applications (from flow past a cylinder to flow past a backward-facing step to the quasi-geostrophic equations[11, 15]). The d2-VMS-ROM is a data-driven ROM closure that leverages the intrinsic hierarchical nature of the ROM basis and the VMS framework [16] to construct data-driven ROM closures. Specifically, the d2-VMS-ROM strategy proceeds by decomposing the ROM space $\mathbf{X}^R := \text{span}\{\varphi_1, \dots, \varphi_R\}$ into the low-dimensional space of large, resolved scales, $\mathbf{X}^r := \text{span}\{\varphi_1, \dots, \varphi_r\}$, and the large-dimensional space of small, unresolved scales, $\mathbf{X}' := \text{span}\{\varphi_{r+1}, \dots, \varphi_R\}$. To ensure computational efficiency, the d2-VMS-ROM is constructed in the low-dimensional space \mathbf{X}^r . However, to ensure numerical accuracy, the d2-VMS-ROM is supplemented with a ROM closure model, τ^{ROM} , which models the effect of the unresolved scales in \mathbf{X}' . We note that one distinguishing feature of the d2-VMS-ROM is that it is built by displaying the explicit formula for the ROM closure term τ^{ROM} , which is achieved by leveraging the VMS formulation. Once we determine the precise form of the ROM closure term, we use one of the two data-driven modeling strategies outlined above (i.e., either a structural or an ML approach) to determine the unknown parameters of the closure model.

In this paper, we consider several d2-VMS-ROM formulations, which are based on linear regression, quadratic manifold formulation, and ML. Furthermore, we also consider a d2-VMS-ROM formulation based on the novel SR-ROM

closure model. To assess the performance of the new SR-ROM closure, we perform an investigation of all four formulations in the numerical simulation of two convection-dominated test problems: flow past a cylinder and lid-driven cavity flow.

The rest of the paper is organized as follows: We begin by introducing the FOM in Section 2. The ROM methodology is presented in Section 3.1. Section 3.2 provides the relevant background information and notation for the VMS approach. We also introduce the novel SR-ROM method along with various ML techniques used to model the closure term for the VMS-ROM, which we refer to as ML-VMS-ROMs. In Section 4, the SR-ROM is compared with the current ML-VMS-ROMs in the numerical simulation of two test problems in the under-resolved, convection-dominated regime: the 2D flow past a cylinder and the 2D lid-driven cavity at Reynolds numbers $\text{Re} = 10000, 15000, \text{ and } 20000$. Concluding remarks are presented in Section 5.

2 Full Order Model (FOM)

The governing equations are the incompressible Navier-Stokes equations (NSE):

$$\frac{\partial \mathbf{u}}{\partial t} + (\mathbf{u} \cdot \nabla) \mathbf{u} = -\nabla p + \frac{1}{\text{Re}} \Delta \mathbf{u}, \quad \nabla \cdot \mathbf{u} = 0. \quad (2.1)$$

Here, \mathbf{u} represents the velocity subject to homogeneous Dirichlet boundary conditions, p denotes the pressure, and Re is the Reynolds number.

We employ the spectral element method for the spatial discretization of (2.1). The P_q - P_{q-2} velocity-pressure coupling [17] is considered, where the velocity \mathbf{u} is represented as a tensor-product Lagrange polynomial of degree q in the reference element $\hat{\Omega} := [-1, 1]^2$, while the pressure p is of degree $q - 2$. This yields a velocity space $\mathbf{X}^{\mathcal{N}}$ for approximating the velocity, and a pressure space $Y^{\mathcal{N}}$ for approximating the pressure, where the finite dimensions \mathcal{N} and $\bar{\mathcal{N}}$ are the global numbers of spectral element degrees of freedom in the corresponding spectral element spaces.

The semi-discretization of (2.1) reads: Find $(\mathbf{u}, p) \in (\mathbf{X}^{\mathcal{N}}, Y^{\mathcal{N}})$ such that, for all $(\mathbf{v}, q) \in (\mathbf{X}^{\mathcal{N}}, Y^{\mathcal{N}})$,

$$\left(\frac{\partial \mathbf{u}}{\partial t}, \mathbf{v} \right) + \left((\mathbf{u} \cdot \nabla) \mathbf{u}, \mathbf{v} \right) = (p, \nabla \cdot \mathbf{v}) - \frac{1}{\text{Re}} (\nabla \mathbf{u}, \nabla \mathbf{v}), \quad (2.2)$$

$$-(\nabla \cdot \mathbf{u}, q) = 0, \quad (2.3)$$

where (\cdot, \cdot) denotes the L^2 inner product. The resulting spatially-discretized ordinary differential equations are solved using a semi-implicit BDFk/EXTk scheme [18]. We refer to [19] for the detailed derivation of the FOM and the treatment with the nonhomogeneous Dirichlet boundary conditions.

3 Reduced Order Models (ROMs)

We present the Galerkin reduced order model (G-ROM) in Section 3.1. In Section 3.2, we first provide background information and establish notation for the VMS-ROM framework. Then, we leverage several ML strategies to construct VMS-ROM closure models. The resulting ROMs, which we collectively call ML-VMS-ROMs, are of four types: the linear regression VMS-ROM (Section 3.2.1); the data-driven VMS-ROM (Section 3.2.2); the novel symbolic regression VMS-ROM (Section 3.2.3); and the neural network VMS-ROM (Section 3.2.4).

3.1 Galerkin ROM (G-ROM)

To construct the G-ROM, we begin by collecting a set of velocity snapshots $\{\mathbf{u}^k := \mathbf{u}(\mathbf{x}, t^k) - \varphi_0\}_{k=1}^K$, which correspond to the FOM solutions at time instances t^k , with the subtraction of the zeroth mode, φ_0 . We then employ the standard proper orthogonal decomposition (POD) procedure [20, 21] to construct the reduced basis functions. The Gramian matrix is formed using the L^2 inner product, and the first r POD basis functions $\{\varphi_i\}_{i=1}^r$ are constructed from the first r eigenmodes of the Gramian.

The G-ROM is constructed by inserting the ROM basis expansion

$$\mathbf{u}_r(\mathbf{x}) = \varphi_0(\mathbf{x}) + \sum_{j=1}^r u_{r,j} \varphi_j(\mathbf{x}) \quad (3.1)$$

into (2.1): Find \mathbf{u}_r such that, for all $\mathbf{v} \in \mathbf{X}_1$,

$$\left(\frac{\partial \mathbf{u}_r}{\partial t}, \mathbf{v}_i \right) + \frac{1}{\text{Re}} (\nabla \mathbf{u}_r, \nabla \mathbf{v}_i) + \left((\mathbf{u}_r \cdot \nabla) \mathbf{u}_r, \mathbf{v}_i \right) = 0, \quad (3.2)$$

where $\mathbf{X}_1 := \text{span}\{\varphi_i\}_{i=1}^r$ is the reduced space.

Remark 3.1. In this paper, the zeroth mode φ_0 is set to be the initial condition of the FOM simulation.

Remark 3.2. We note that, in the case of fixed geometries, the divergence and pressure terms drop out of (3.2) since the ROM basis is weakly divergence-free. For ROMs that include the pressure approximation, see, e.g., [1, 2, 22, 23, 24].

From (3.2), a system of differential equations in the coefficients of the POD bases, $u_{r,j}$, is derived:

$$B \frac{d\mathbf{u}_r}{dt} = -\mathcal{C}(\mathbf{u}_r) \mathbf{u}_r - \frac{1}{\text{Re}} A \mathbf{u}_r, \quad (3.3)$$

where $\mathbf{u}_r \in \mathbb{R}^r$ is the vector of POD coefficients $\{u_{r,j}\}_{j=1}^r$, and $\mathbf{u}_r \in \mathbb{R}^{r+1}$ is the augmented vector that includes the zeroth mode's coefficient. A , B , and C represent the reduced stiffness, mass, and advection operators, respectively, with entries

$$A_{ij} = \int_{\Omega} \nabla \varphi_i : \nabla \varphi_j dV, \quad B_{ij} = \int_{\Omega} \varphi_i \cdot \varphi_j dV, \quad C_{ikj} = \int_{\Omega} \varphi_i \cdot (\varphi_k \cdot \nabla) \varphi_j dV. \quad (3.4)$$

For temporal discretization of (3.3), a semi-implicit scheme with k th-order backward differencing (BDF k) and k th-order extrapolation (EXT k) is considered. The fully discretized reduced system at time t^l is then derived:

$$\left(\frac{\beta_0}{\Delta t} B + \frac{1}{\text{Re}} A \right) \mathbf{u}_r^{l+1} = - \sum_{i=1}^k \alpha_i [\mathcal{C}(\mathbf{u}_r^{l-i}) \mathbf{u}_r^{l-i} + (C_1 + C_2) \mathbf{u}_r^{l-i} - \mathbf{c}_0] - B \sum_{i=1}^k \frac{\beta_i}{\Delta t} \mathbf{u}_r^{l-i} - \frac{1}{\text{Re}} \mathbf{a}_0, \quad (3.5)$$

where

$$c_{0,i} = \int_{\Omega} \varphi_i \cdot (\varphi_0 \cdot \nabla) \varphi_0 dV, \quad a_{0,i} = \int_{\Omega} \nabla \varphi_i : \nabla \varphi_0 dV, \quad (3.6)$$

$$C_{1,ij} = \int_{\Omega} \varphi_i \cdot (\varphi_0 \cdot \nabla) \varphi_j dV, \quad C_{2,ik} = \int_{\Omega} \varphi_i \cdot (\varphi_k \cdot \nabla) \varphi_0 dV, \quad (3.7)$$

for all $i = 1, \dots, r$ and $j, k = 0, \dots, r$.

3.2 Machine Learning Variational Multiscale ROMs (ML-VMS-ROMs)

The variational multiscale (VMS) methods are numerical discretization techniques that greatly enhance the accuracy of classical Galerkin approximations in under-resolved simulations. This situation often occurs with coarse meshes or when there are insufficient basis functions available. The VMS framework, originally proposed by Hughes and his colleagues [25], has significantly influenced various fields in computational mechanics. For comprehensive reviews of its impact, see [26, 27].

In the following, we describe the VMS-ROM framework [11]. First, we consider two reduced spaces $\mathbf{X}_1 := \text{span}\{\varphi_1, \dots, \varphi_r\}$ and $\mathbf{X}_2 := \text{span}\{\varphi_{r+1}, \dots, \varphi_R\}$, where φ_i is the i -th reduced basis function, and R is the dimension of the snapshot dataset. We note that \mathbf{X}_1 represents the span of the resolved ROM scales, and \mathbf{X}_2 represents the span of the unresolved scales. In addition, the two reduced spaces are orthogonal because of the POD construction.

Next, we use the best ROM approximation of \mathbf{u} in the space $\mathbf{X}_1 \oplus \mathbf{X}_2$, that is, $\mathbf{u}_R \in \mathbf{X}_1 \oplus \mathbf{X}_2$, defined as

$$\mathbf{u}_R = \sum_{j=1}^R u_{r,j} \varphi_j(\mathbf{x}) = \sum_{j=1}^r u_{r,j} \varphi_j + \sum_{j=r+1}^R u_{r,j} \varphi_j = \mathbf{u}_r + \mathbf{u}'_r, \quad (3.8)$$

where $\mathbf{u}_r \in \mathbf{X}_1$ represents the resolved ROM component of \mathbf{u} , and $\mathbf{u}'_r \in \mathbf{X}_2$ represents the unresolved ROM component of \mathbf{u} .

Plugging \mathbf{u}_R in (2.1) and projecting the resulting equation onto \mathbf{X}_1 , we obtain

$$\left(\frac{\partial \mathbf{u}_R}{\partial t}, \mathbf{v}_i \right) + \frac{1}{\text{Re}} (\nabla \mathbf{u}_R, \nabla \mathbf{v}_i) + \left((\mathbf{u}_R \cdot \nabla) \mathbf{u}_R, \mathbf{v}_i \right) = 0, \quad \forall i = 1, \dots, r. \quad (3.9)$$

Using the orthogonality of the ROM basis functions, one can show that

$$\left(\frac{\partial \mathbf{u}_R}{\partial t}, \mathbf{v}_i\right) = \left(\frac{\partial \mathbf{u}_r}{\partial t}, \mathbf{v}_i\right), \quad \forall i = 1, \dots, r, \quad (3.10)$$

and (3.9) can be further written as: $\forall i = 1, \dots, r$

$$\begin{aligned} & \left(\frac{\partial \mathbf{u}_r}{\partial t}, \mathbf{v}_i\right) + \frac{1}{\text{Re}} (\nabla \mathbf{u}_r, \nabla \mathbf{v}_i) + \left((\mathbf{u}_r \cdot \nabla) \mathbf{u}_r, \mathbf{v}_i\right) \\ & + \left[\frac{1}{\text{Re}} (\nabla \mathbf{u}_R, \nabla \mathbf{v}_i) + \left((\mathbf{u}_R \cdot \nabla) \mathbf{u}_R, \mathbf{v}_i\right) - \frac{1}{\text{Re}} (\nabla \mathbf{u}_r, \nabla \mathbf{v}_i) - \left((\mathbf{u}_r \cdot \nabla) \mathbf{u}_r, \mathbf{v}_i\right) \right] = 0. \end{aligned} \quad (3.11)$$

The bracketed term in (3.11) is the VMS-ROM closure term, which models the interaction between the ROM modes $\{\varphi_1, \dots, \varphi_r\}$ and the discarded ROM modes $\{\varphi_{r+1}, \dots, \varphi_R\}$.

Equation (3.11) is referred to as VMS-ROM and can be written as:

$$B \frac{d\mathbf{u}_r}{dt} = -\mathcal{C}(\underline{\mathbf{u}}_r) \underline{\mathbf{u}}_r - \frac{1}{\text{Re}} A \underline{\mathbf{u}}_r + \underline{\tau}_{\text{VMS}}, \quad (3.12)$$

where

$$\tau_{\text{VMS},i} \equiv \left((\mathbf{u}_R \cdot \nabla) \mathbf{u}_R, \varphi_i\right) - \left((\mathbf{u}_r \cdot \nabla) \mathbf{u}_r, \varphi_i\right), \quad \forall i = 1, \dots, r. \quad (3.13)$$

Remark 3.3. If we drop the VMS-ROM closure term, we are left with the G-ROM (3.2).

Remark 3.4. The VMS-ROM closure term is a correction term in the higher-dimensional space $\mathbf{X}_1 \oplus \mathbf{X}_2$.

The VMS-ROM closure term τ_{VMS} is essential for the accuracy of (3.12). However, the unresolved component of \mathbf{u}_R , \mathbf{u}'_r , is not available during the online stage. To overcome this issue, for each $i = 1, \dots, r$, $\tau_{\text{VMS},i}$ is approximated using a generic function $g_i(\underline{\mathbf{u}}_r)$ as follows:

$$\tau_{\text{VMS},i} \equiv \left((\mathbf{u}_R \cdot \nabla) \mathbf{u}_R, \varphi_i\right) - \left((\mathbf{u}_r \cdot \nabla) \mathbf{u}_r, \varphi_i\right) \approx g_i(\underline{\mathbf{u}}_r). \quad (3.14)$$

In the VMS-ROM training, for each $i = 1, \dots, r$, the function g_i is determined by minimizing the mean squared error (MSE) between the VMS-ROM closure τ_i and the reconstruction made by g_i ,

$$\text{MSE}_{\text{tr},i} := \frac{1}{N_{\text{tr}}} \sum_{j=1}^{N_{\text{tr}}} (\tau_i^j - g_i(\widehat{\underline{\mathbf{u}}}_r^j))^2. \quad (3.15)$$

We note that N_{tr} is the number of training time samples, which, in our numerical experiments, is selected to be the same as the number of snapshots that are used to build the POD basis functions. The VMS-ROM closure term τ_i^j is defined to be

$$\tau_i^j \equiv \left((\mathcal{P}_R \mathbf{u}^j \cdot \nabla) \mathcal{P}_R \mathbf{u}^j, \varphi_i\right) - \left((\mathcal{P}_r \mathbf{u}^j \cdot \nabla) \mathcal{P}_r \mathbf{u}^j, \varphi_i\right), \quad (3.16)$$

where \mathcal{P}_r is the operator that projects the FOM solution $\mathbf{u} \in \mathbf{X}^N$ onto the r -dimensional reduced space \mathbf{X}_r , and \mathbf{u}^j is the FOM solution at time t^j . The vector of ROM coefficients $\widehat{\underline{\mathbf{u}}}_r$ is obtained by projecting the FOM solution onto the r -dimensional reduced space, that is, $\widehat{\underline{\mathbf{u}}}_{r,i}^j = (\mathbf{u}^j, \varphi_i)$ for all $i = 1, \dots, r$. We note that for $i = 1, \dots, r$, the function g_i is found independently.

Remark 3.5. By a slight abuse of notation, we refer to both (3.13) and (3.16) as the VMS-ROM closure term. We note that (3.16) is used to train the function g_i instead of (3.13) because the latter requires running the R -dimensional G-ROM, which is not practical. Moreover, the stiffness terms are ignored in both (3.13) and (3.16) because these terms are usually small in the convection-dominated regime due to the $1/\text{Re}$ scaling (see the careful discussion of the commutation error in [28]).

In the remainder of this section, we describe the four ML techniques that we employ to construct the function g_i in the ML-VMS-ROMs: the linear regression VMS-ROM (outlined in Section 3.2.1); the data-driven VMS-ROM (outlined in Section 3.2.2); the novel symbolic regression VMS-ROM (outlined in Section 3.2.3); and the neural network VMS-ROM (outlined in Section 3.2.4). A schematic of the four different ROM closure modeling strategies that are used to construct the ML-VMS-ROMs is depicted in Figure 3.1.

If one considers a zeroth mode in the definition of \mathbf{u}_R and \mathbf{u}_r , the zeroth mode contribution will not appear in the VMS-ROM closure term because of the cancellation.

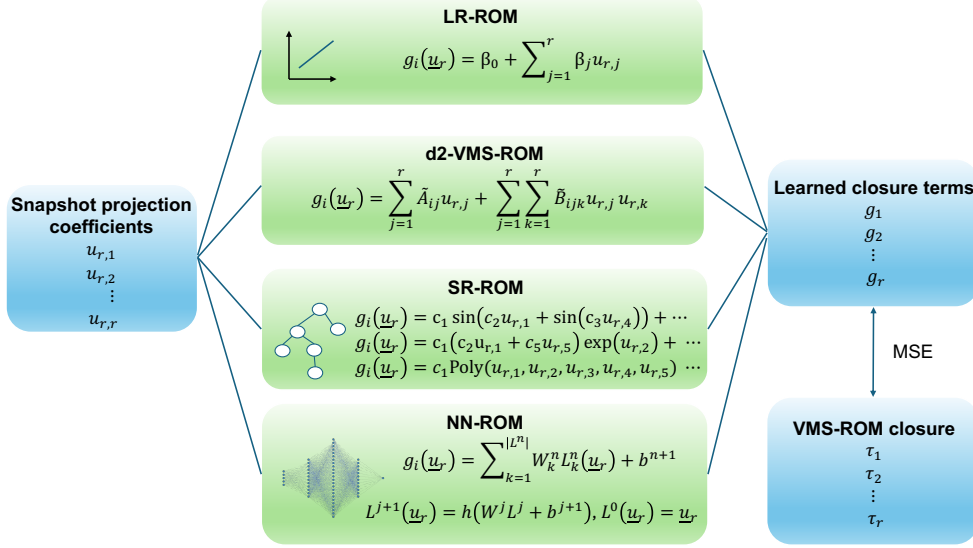


Figure 3.1: Schematic of the ML-VMS-ROMs considered in this paper.

3.2.1 VMS-ROM with Linear Regression Closure Models (LR-ROM)

Linear regression (LR) predicts a target (dependent) variable y (in our case, the i -th component of the VMS ROM closure, τ_i) based on one or more input (independent) variables x_j (in our case, the j -th ROM coefficient, $u_{r,j}$) by assuming a linear dependency between them. Mathematically, for each $i = 1, \dots, r$, the function g_i is postulated as

$$g_i(\underline{u}_r) = \beta_0 + \sum_{j=1}^r \beta_j u_{r,j}, \quad (3.17)$$

where r is the dimension of the reduced space and $(\beta_0, \dots, \beta_r)$ are the learnable weights. The optimal weights are found by solving the linear system given by the normal equations (see equation (2.5) in [29]). To penalize the complexity of the model and avoid overfitting, the regularization term $\alpha \sum_{j=1}^r \beta_j^2$ is added to (3.15) to favor the solution with weights of smaller L^2 norm.

In this work, the Ridge class of the `scikit-learn` library is used for training the LR-ROM. The default settings are used, apart for the hyperparameter α , which is tuned through a hold-out validation based on the error metric (4.2). A more detailed discussion on LR can be found in [30]. The advantages of LR stem from its interpretability and simplicity. However, linear models may not always effectively describe data, and they are particularly sensitive to outliers.

3.2.2 Data-Driven Variational Multiscale ROMs (d2-VMS-ROM)

In [11], the authors proposed a data-driven approach to approximate the VMS-ROM closure. In particular, the structure of function g_i is assumed to be similar to the structure of the G-ROM function and is postulated as

$$g_i(\underline{u}_r) = \sum_{j=1}^r \tilde{A}_{ij} u_{r,j} + \sum_{j=1}^r \sum_{k=1}^r \tilde{B}_{ijk} u_{r,j} u_{r,k}. \quad (3.18)$$

The entries in the $r \times r$ matrix \tilde{A} and the $r \times r \times r$ tensor \tilde{B} are determined by minimizing the training MSE (3.15). We note that the minimization problem is equivalent to the following least squares problem

$$\min_{\underline{x}} \|G\underline{x} - \underline{f}\|^2, \quad (3.19)$$

where $G \in \mathbb{R}^{N_{\text{tr}} \times (r^2 + r^3)}$ is a matrix whose entries are determined by \hat{u}_r^j , for $j = 1, \dots, N_{\text{tr}}$, $\underline{f} \in \mathbb{R}^{N_{\text{tr}} \times r}$ is a vector whose entries are determined by τ^j for $j = 1, \dots, N_{\text{tr}}$, and $\underline{x} \in \mathbb{R}^{(r^2 + r^3) \times 1}$ is a vector whose entries are determined by \tilde{A} and \tilde{B} . To alleviate the ill-conditioning of the least squares problem (3.19) [31], we use the truncated SVD as a regularization method [11].

3.2.3 VMS-ROM with Symbolic Regression Closure Models (SR-ROM)

Symbolic regression (SR) is a type of regression analysis that seeks to find mathematical expressions that accurately describe the relationship between the features and the labels of a dataset [32]. Unlike traditional regression methods, which rely on predefined model structures, SR identifies both the structure of the model and its parameters.

Here, we use SR to search for the function g_i in (3.14) that solves the following optimization problem

$$g_i = \arg \max_{f \in \mathcal{F}} \left[1 - \frac{\sum_{j=1}^{N_{tr}} (\tau_i^j - f(\hat{u}_r^j))^2}{\sum_{j=1}^{N_{tr}} (\tau_i^j - \bar{\tau}_i)^2} \right], \quad (3.20)$$

where $\bar{\tau}_i$ is the mean of τ_i over N_{tr} samples and \mathcal{F} is a set of functions generated by a *primitive set*, that is, a collection of mathematical operations, such as $\{+, -, *, \sin, \exp\}$, and a *terminal set*, made of the independent variables and some constants. We note that maximizing the objective function in (3.20) (called *fitness*) is equivalent to minimizing the MSE in (3.15). Apart from dealing with algebraic expressions, SR has recently been extended to field problems by including discrete differential operators [33].

A common approach to SR (also adopted in this work) is genetic programming (GP) [34, 35]. GP is a gradient-free strategy that explores a space of mathematical expressions by iteratively evolving a population of candidate models through genetic operations. A candidate model, is also known as *individual*, can be represented by a tree, where each node is either a *primitive* or a *terminal* (i.e., a variable or a constant), and is characterized by its *fitness*, as defined above. GP-based SR consists of the following steps:

1. An initial population of individuals is randomly generated, based on the chosen primitive set;
2. For each individual, the constants are optimized via the Levenberg–Marquardt method to maximize the fitness function;
3. A pool of individuals are *selected* according to fitness-based tournaments. Specifically, for each tournament a given number (tournament size) of individuals are sampled from the population and the ones with the highest fitness are selected for the next step;
4. The selected expressions are modified using *crossover* (combining parts of two parent expressions to create new offspring) and *mutation* (randomly altering parts of an expression);
5. Steps 2–4 are repeated for multiple *generations*, until a stopping condition is satisfied or a maximum number of generations is reached.

A more detailed review of SR methods can be found in [34, 35]. A schematic of the described algorithm is reported in Figure 3.2.

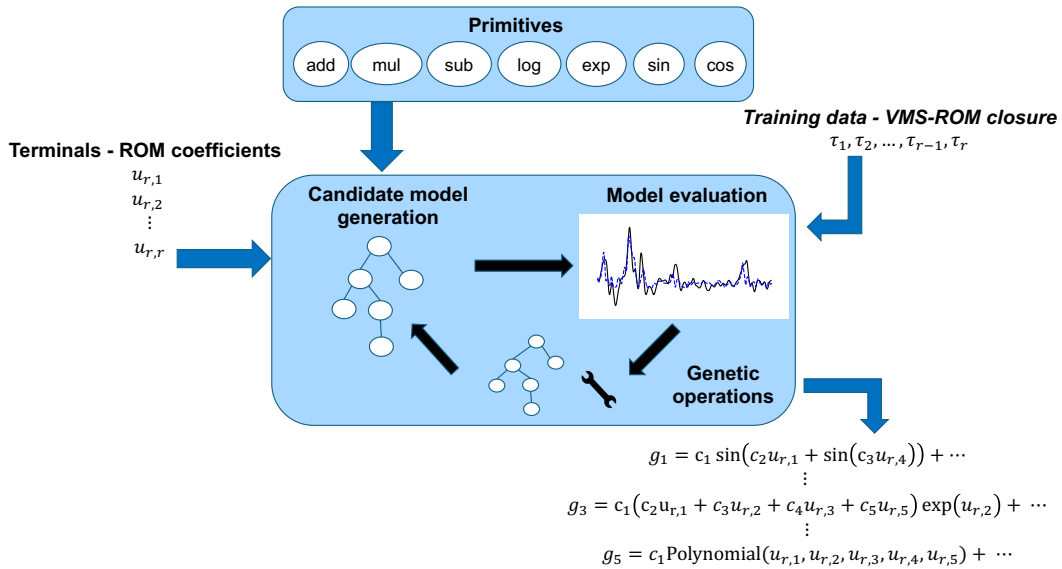


Figure 3.2: Schematic of the symbolic regression approach used to model ROM closures (SR-ROM).

In this paper, we used the SR implementation of the `pyoperon` [36] library, because it achieves a good compromise between test performance, final model size, and training time (see, e.g., Figure 1 in [37]). We fixed the following hyperparameters for every run:

- tournament size equal to 5;
- number of iterations of the constant optimizer equal to 10;
- population size equal to 1000;
- maximum depth of the trees equal to 5.

The maximum length of the individuals (i.e., the number of nodes), the number of generations, and the primitive set were tuned through a grid search based on a hold-out validation. A description of the datasets used for training, validation, and testing can be found in Section 4.

3.2.4 VMS-ROM with Neural Network Closure Models (NN-ROM)

Among the different architectures of neural networks (NNs), in this work, we used a multi-layer perceptron (MLP) to represent the mapping between the vector of ROM coefficients \underline{u}_r and the approximated closure term. The MLP can be represented mathematically as follows:

$$g_i(\underline{u}_r) := \sum_{k=1}^{|L^n|} W_k^n L_k^n(\underline{u}_r) + b^{n+1}, \quad (3.21)$$

$$L^{j+1}(\underline{u}_r) := h(W^j L^j + b^{j+1}), \quad 0 \leq j \leq n-1, \quad (3.22)$$

$$L^0(\underline{u}_r) := \underline{u}_r, \quad (3.23)$$

where n is the number of the (hidden) layers, L^j is the output of the j -th layer, $|L^n|$ is the number of nodes of the n -th layer, h is the activation function, W^j is the weight matrix for the connections between the j -th and the $(j+1)$ -th layers, and b^j is the bias term for the outputs of the j -th layer.

The training of the NN amounts to adjusting its weights to minimize a loss function using *backpropagation* [38]. Here, as a loss function, we chose the sum of the MSE (3.15) and the L^2 regularization term, which penalizes the sum of the squares of the weights. A more detailed introduction to NNs can be found in [39, 30].

In this work, we used the `skorch` [40] library for training the MLP with the following settings:

- LeakyReLU as the activation function;
- Adam optimizer;
- 100 training epochs;
- batch size equal to 512.

We tuned the values of the learning rate, the number of units per layer, the L^2 regularization parameter, and the dropout rate through a grid search based on a hold-out validation. Details on the datasets used for training, validation, and testing can be found in Section 4.

4 Numerical Results

In this section, we assess the four ML-VMS-ROMs introduced in Section 3.2 in the numerical simulation of two test problems: (i) the 2D flow past a cylinder, and (ii) the 2D lid-driven cavity. We emphasize that, for both test problems, we consider the under-resolved regime, i.e., the case when the number of ROM basis functions is not large enough to capture the underlying dynamics. We also note that, for the 2D lid-driven cavity, we consider the convection-dominated regime. Both the under-resolved regime and the convection-dominated regime are relevant to the realistic engineering and geophysical settings (e.g., the numerical simulation of turbulent flows).

We remark that each model depends on hyperparameters, and we list the considered hyperparameters for each model below. In each model, the function g_i is determined by minimizing the training MSE, $\text{MSE}_{\text{tr},i}$ (3.15).

- For the LR-ROM, we select the L^2 regularization parameter from the set $\{10^i, 2 \times 10^i, \dots, 9 \times 10^i\}_{i=0, \dots, 5}$.

- For the d2-VMS-ROM, we select the SVD rank from the set $\{1, 2, \dots, \text{Rank}(G)\}$, where G is the matrix in the least squares problem (3.19), whose entries are determined by the ROM coefficients of the projected snapshots, $\hat{\underline{u}}_r$.
- For the SR-ROM, we select the maximum length from the set $\{5, 10, \dots, 45, 50\}$, the number of generations from the set $\{10, 25, 50, 75, 100\}$, and the primitive set from the set $\{\{\text{add, sub, mul, constant, variable}\}, \{\text{add, sub, mul, sin, constant, variable}\}, \{\text{add, sub, mul, exp, sin, constant, variable}\}, \{\text{add, sub, mul, sin, cos, constant, variable}\}, \{\text{add, sub, mul, exp, sin, cos, constant, variable}\}, \{\text{add, sub, mul, exp, sin, cos, square, log, constant, variable}\}\}$;
- For the NN-ROM, we select the learning rate from the set $\{10^{-4}, 10^{-3}, 10^{-2}\}$, the number of nodes per layer from the set $\{[64, 128, 256, 512, 256, 128, 64], [64, 128, 256, 128, 64], [64, 128, 64]\}$, the L^2 regularization parameter from the set $\{10^{-5}, 10^{-4}, 10^{-3}\}$, and the dropout rate from the set $\{0.3, 0.4, 0.5\}$.

For each model and each hyperparameter, the selected function g_i is then integrated with the VMS-ROM, and its performance is further evaluated in the validation interval. The optimal hyperparameters are selected to be those that maximize the coefficient of determination

$$R_{\text{val}}^2 := 1 - \frac{\text{MSE}_{\text{val}}}{\frac{1}{N_{\text{val}}} \sum_{i=1}^{N_{\text{val}}} (E_{\text{FOM}}^i - \overline{E}_{\text{FOM}})^2}, \quad (4.1)$$

where the validation error, MSE_{val} , is defined to be the MSE between the FOM kinetic energy and the ROM kinetic energy,

$$\text{MSE}_{\text{val}} = \frac{1}{N_{\text{val}}} \sum_{i=1}^{N_{\text{val}}} (E_{\text{FOM}}^i - E_{\text{ROM}}^i)^2. \quad (4.2)$$

The kinetic energy E at time t^j is defined to be

$$E(t^j) = E^j = \frac{1}{2} \left(\int_{\Omega} \mathbf{u}^j \cdot \mathbf{u}^j d\Omega \right)^{\frac{1}{2}}, \quad (4.3)$$

and the averaged kinetic energy over the N_{val} samples in the validation set is defined to be

$$\overline{E}_{\text{FOM}} = \frac{1}{N_{\text{val}}} \sum_{i=1}^{N_{\text{val}}} E_{\text{FOM}}^i. \quad (4.4)$$

Once the optimal parameters are selected, the resulting ML-VMS-ROM is assessed in a testing interval with the metric

$$\text{rMSE}_{\text{test}} := \frac{1}{N_{\text{test}}} \sum_{i=1}^{N_{\text{test}}} \frac{(E_{\text{FOM}}^i - E_{\text{ROM}}^i)^2}{(E_{\text{FOM}}^i)^2}. \quad (4.5)$$

4.1 2D Flow Past a Cylinder

Our first test problem is the 2D flow past a cylinder, which is a canonical test case for ROMs. The computational domain is $\Omega = [-2.5D : 17D] \times [-5D : 5D]$, where D is the cylinder diameter, and the cylinder is centered at $[0, 0]$. We consider two Reynolds numbers, namely, $\text{Re} = 400$ and $\text{Re} = 500$. For each Reynolds number, we collect $N_{\text{tr}} = 2001$ snapshots, $\{\mathbf{u}^k := \mathbf{u}(\mathbf{x}, t^k) - \boldsymbol{\varphi}_0\}_{k=1}^{N_{\text{tr}}}$, over the time interval $[500, 520]$ (measured in convective time units, D/U , where U is the free-stream velocity). These snapshots are taken after the von Karman vortex street has developed, with sampling time $\Delta t_s = 0.01$. The zeroth mode, $\boldsymbol{\varphi}_0$, is set to be the FOM velocity field at $t = 500$. Snapshots of the velocity magnitude for $\text{Re} = 400$ and $\text{Re} = 500$ are displayed in Fig. 4.1.

The snapshot data are then used to construct the reduced basis functions $\{\boldsymbol{\varphi}_i\}_{i=1}^r$ by using POD. The ROM coefficients, $\{\hat{\underline{u}}_r^j\}_{j=1}^{N_{\text{tr}}}$, are computed by projecting the snapshots onto the R -dimensional reduced space, where R is the rank of the snapshot matrix. The VMS-ROM closure terms $\{\mathcal{T}^j\}_{j=1}^{N_{\text{tr}}}$ are then computed using (3.16). For each ML-VMS-ROM, the function g_i is found by minimizing the training MSE (3.15). We select the optimal values for the hyperparameters for model training such that they minimize the validation error (4.2). To evaluate this error, we further run the FOM simulation and monitor the FOM kinetic energy over the time interval $[520, 540]$. The trained function g_i is then used within the VMS-ROM to perform a simulation over the time interval $[500, 540]$. Finally, we assess the generalization error in (4.5) of all the ROMs in an extrapolation region, that is, in the time interval $[540, 600]$.

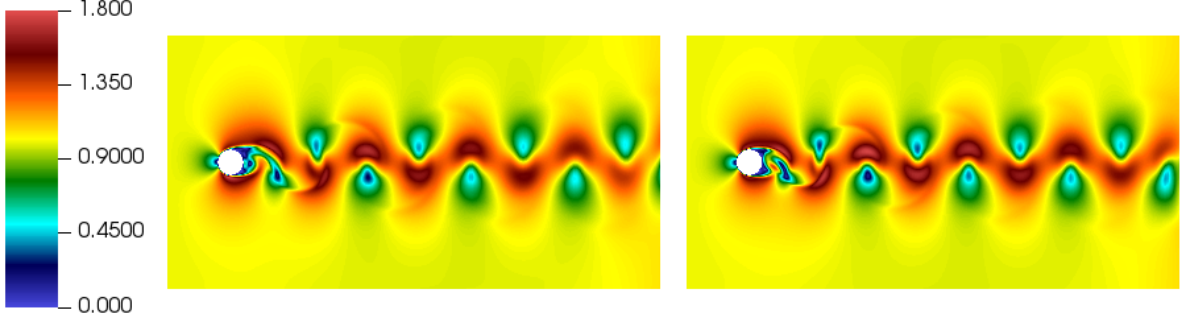


Figure 4.1: 2D flow past a cylinder. Velocity magnitude snapshots for $\text{Re} = 400$ (left) and $\text{Re} = 500$ (right).

In Table 1, the relative MSE ($\text{rMSE}_{\text{test}}$) between the FOM kinetic energy and the predicted kinetic energy during the time interval $[540, 600]$ (extrapolation region) for all the ML-VMS-ROMs is reported with respect to the reduced space dimension $r = 2, 3, 4, 5$. Because the models trained using neural networks and symbolic regression rely on stochastic optimization algorithms, the $\text{rMSE}_{\text{test}}$ for both the NN-ROM and the SR-ROM are computed by averaging the results over 5 runs corresponding to different seeds. The results show that the SR-ROM is the most robust model with respect

Table 1: 2D flow past a cylinder. Relative MSE ($\text{rMSE}_{\text{test}}$) between the FOM kinetic energy and the kinetic energy predicted in the extrapolation region (*i.e.*, in the time interval $[540, 600]$) by the ML-VMS-ROMs, for different values of the reduced space dimension $r = 2, 3, 4, 5$. For the SR-ROM and the NN-ROM, the mean and the standard deviation over 5 independent runs (different seeds) are reported. In bold, the best performing model for each r value is listed.

Re	r	LR-ROM	d2-VMS-ROM	SR-ROM	NN-ROM
400	2	1.4×10^{-4}	5.3×10^{-6}	$(7.1 \pm 1.1) \times 10^{-7}$	$(5.3 \pm 3.7) \times 10^{-6}$
	3	3.3×10^{-4}	nan	$(1.5 \pm 2.0) \times 10^{-5}$	$(3.1 \pm 3.1) \times 10^{-4}$
	4	5.5×10^{-5}	7.5×10^{-7}	$(6.7 \pm 1.0) \times 10^{-7}$	$(4.4 \pm 2.7) \times 10^{-6}$
	5	4.6×10^{-6}	2.0×10^{-5}	$(9.5 \pm 8.9) \times 10^{-7}$	$(10.0 \pm 6.7) \times 10^{-7}$
500	2	8.1×10^{-6}	3.2×10^{-5}	$(1.7 \pm 1.9) \times 10^{-5}$	$(4.5 \pm 1.6) \times 10^{-6}$
	3	6.6×10^{-5}	3.7×10^{-5}	$(1.8 \pm 1.0) \times 10^{-6}$	$(2.7 \pm 1.6) \times 10^{-6}$
	4	2.2×10^{-5}	3.2×10^{-6}	$(7.2 \pm 5.1) \times 10^{-6}$	$(10.4 \pm 7.8) \times 10^{-6}$
	5	3.1×10^{-4}	1.9×10^{-4}	$(1.0 \pm 1.3) \times 10^{-6}$	$(4.7 \pm 2.3) \times 10^{-5}$

to r for both Re , followed by the NN-ROM, the d2-VMS-ROM, and the LR-ROM. In particular, we note that for $\text{Re} = 400$ and $r = 2$ and $r = 3$ the SR-ROM $\text{rMSE}_{\text{test}}$ values in the extrapolation region are an order of magnitude lower than the $\text{rMSE}_{\text{test}}$ values of the other ROMs. The same happens for $\text{Re} = 500$ and $r = 5$.

We further measure the closeness between the VMS-ROM closure terms $\{\tau^j\}_{j=1}^{N_{\text{tr}}}$ and the reconstructed closure terms for each model. In particular, the MSE for each τ component, $\text{MSE}_{\text{tr},i}$ (3.15) is computed, and the mean MSE, which is defined as

$$\overline{\text{MSE}}_{\text{tr}} := \frac{1}{r} \sum_{i=1}^r \text{MSE}_{\text{tr},i}, \quad (4.6)$$

is reported in Table 2. We observe that SR-ROM is the most robust method also in this case. We also note that the NN-ROM has a much larger MSE than the SR-ROM even though the corresponding test errors on predicted energy are comparable (Table 1). For example, for $\text{Re} = 500$, the training MSE of NN-ROM with $r = 3$ is roughly two orders of magnitude larger than the training MSE of SR-ROM. However, the performance of the two models in the extrapolation region is comparable. There are two reasons for this behavior:

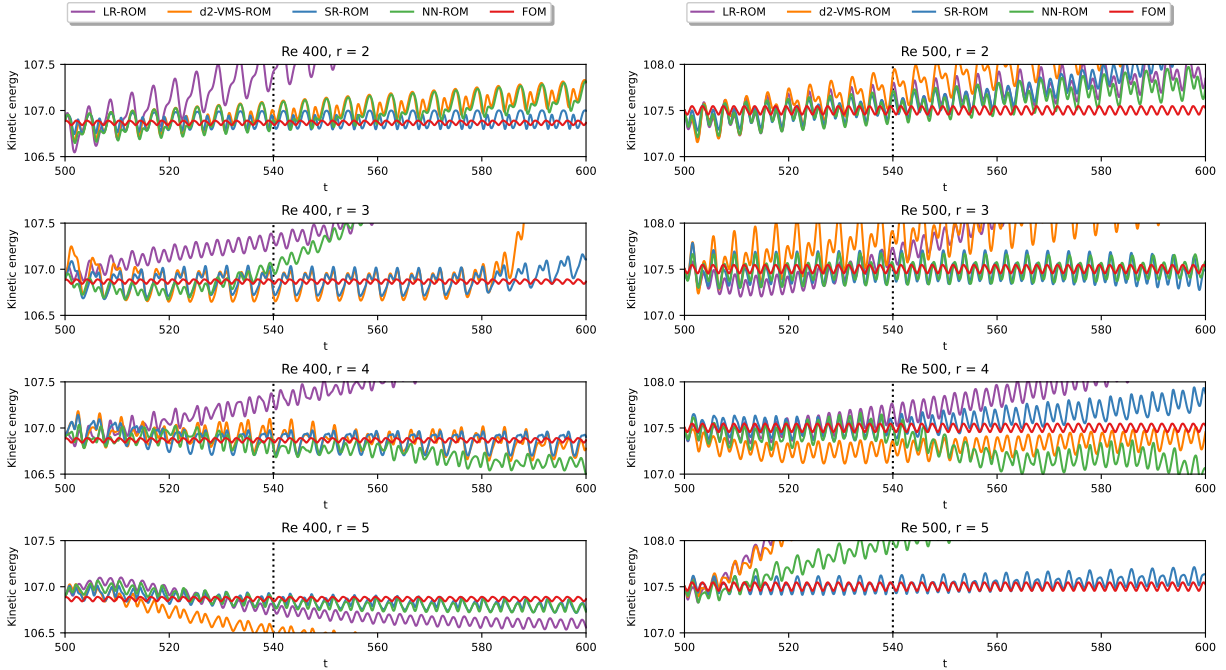
1. We are using different metrics for training (closure error) and validation/testing (kinetic energy error).
2. In the NN-ROM and LR-ROM, we consider L^2 regularization to prevent models from overfitting. This results in a model with smaller weights and could lead to a larger training MSE but better generalizability (smaller $\text{rMSE}_{\text{test}}$ in the extrapolation region).

Overall, our results demonstrate that, SR-ROM outperforms the other ML-VMS-ROM models in terms of generalizability.

Table 2: 2D flow past a cylinder. Mean squared error ($\overline{\text{MSE}_{\text{tr}}}$) between the VMS-ROM closure and the closures given by the ML-VMS-ROMs for $\text{Re} = 400, 500$. In bold, the best performing model for each case is listed.

Re	r	LR-ROM	d2-VMS-ROM	SR-ROM	NN-ROM
400	2	2.3×10^{-3}	5.2×10^{-4}	$(6.9 \pm 12.5) \times 10^{-7}$	$(8.5 \pm 4.6) \times 10^{-4}$
	3	5.9×10^{-3}	5×10^{-4}	$(1.3 \pm 2.6) \times 10^{-4}$	$(1.7 \pm 1.1) \times 10^{-3}$
	4	3.1×10^{-3}	6.1×10^{-4}	$(1.2 \pm 1.5) \times 10^{-4}$	$(1.2 \pm 0.5) \times 10^{-3}$
	5	1.4×10^{-3}	5.6×10^{-6}	$(5.7 \pm 4.9) \times 10^{-5}$	$(1.9 \pm 0.4) \times 10^{-4}$
500	2	4.7×10^{-4}	1.2×10^{-3}	$(5.5 \pm 3.3) \times 10^{-5}$	$(8.7 \pm 4.3) \times 10^{-5}$
	3	5.9×10^{-3}	3.5×10^{-4}	$(7.5 \pm 12) \times 10^{-6}$	$(5.5 \pm 3.6) \times 10^{-4}$
	4	3.5×10^{-3}	4.1×10^{-3}	$(1.4 \pm 2.7) \times 10^{-4}$	$(4.9 \pm 2.7) \times 10^{-4}$
	5	1.0×10^{-3}	4×10^{-4}	$(5.2 \pm 3.0) \times 10^{-5}$	$(8 \pm 6.1) \times 10^{-4}$

In Fig. 4.2, we show the kinetic energy behavior of the ROMs and the FOM in the time interval $[500, 600]$ with reduced space dimension $r = 2, 3, 4, 5$ for $\text{Re} = 400$ and $\text{Re} = 500$. For $\text{Re} = 400$, we observe that the LR-ROM energy deviates away from the FOM energy for all r values considered. For the d2-VMS-ROM and the NN-ROM, although the energy is better than the LR-ROM energy, it could still deviate away from the FOM energy; see, for example, the $r = 3$ case. The SR-ROM is the most stable compared to the other three ML-VMS-ROMs, and it is able to predict energy that is comparable to the FOM energy. For $\text{Re} = 500$, we again observe that the LR-ROM energy deviates


 Figure 4.2: 2D flow past a cylinder at $\text{Re} = 400$ and $\text{Re} = 500$. Comparison of the kinetic energy of the FOM and the ROMs for the reduced space dimension $r = 2, 3, 4, 5$.

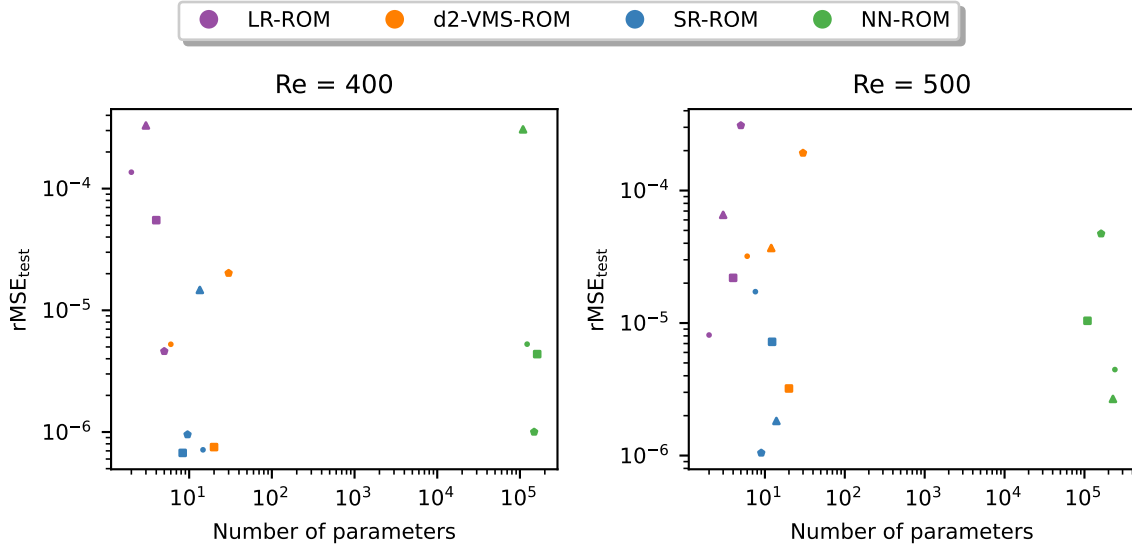
away from the FOM energy for all r values considered. For the d2-VMS-ROM and the NN-ROM, although the energy is better than the LR-ROM energy, it could still deviate away from the FOM energy; see, for example, the $r = 5$ case. The SR-ROM is the most stable with respect to different r values.

In Table 3, we report the best symbolic models in terms of the $\text{rMSE}_{\text{test}}$ for both Reynolds numbers. We observe that all the expressions are simple and compact.

In Figure 4.3, we further plot the $\text{rMSE}_{\text{test}}$ as a function of the number of parameters for each ROM. We note that the number of constants is reported for the SR-ROM and the number of weights for the other ROMs. We remark that the

Table 3: 2D flow past a cylinder. Expressions of the components of the SR-ROM closure model that attains the minimum $\text{rMSE}_{\text{test}}$ in the extrapolation region reported in Table 1.

Re	Component	Expression
400	g_1	$(-0.039u_1 + 0.002u_2 - 0.034) \sin(1.719u_2 - 3.789) + 0.000$
	g_2	$(-0.077u_1 + 0.031u_4 - 0.073) \sin(1.062u_1 - 1.804u_2) + 0.020$
	g_3	$-0.384u_1 + 0.384u_3 + 0.039u_4 + 0.971 \sin(1.868u_1 + 0.123) - 0.012$
	g_4	$(7.533u_2 - 1.921u_4)(0.706u_2 + 0.046u_4 - \sin(0.846u_2)) - 0.008$
500	g_1	$0.015u_1 + 0.010u_4 + \sin(0.191u_1 - 0.100u_5 + \sin(0.064u_4) - 1.569) + 0.979$
	g_2	$1.004(0.264u_2u_3 - \exp(0.282u_2))(0.007u_1 - 0.005u_2 - 0.014u_3 + 0.006u_4) - 0.002$
	g_3	$-0.999(0.033u_1 - 0.005u_5)(1.795u_2 - 2.109u_5) - (0.040u_1 - 0.042) \exp(1.895u_1)$
	g_4	$-0.999(0.009u_1 - 0.004u_5 + 0.009)(1.449u_2 + 3.357u_3 + 1.044u_5 + 2.355)$
	g_5	$-0.017u_1 - 0.013u_3^2 + 0.011u_5 + 0.852(0.001u_1 - 0.001u_5)(17.071u_4 - 31.025u_5) - 0.009$


 Figure 4.3: 2D flow past a cylinder. $\text{rMSE}_{\text{test}}$ as a function of the number of parameters of the model. For the SR-ROM and the NN-ROM, the mean values out of 5 independent runs are reported. Each point is marked using the following legend: point for $r = 2$; triangle for $r = 3$; square for $r = 4$; pentagon for $r = 5$.

d2-VMS-ROM results for $\text{Re} = 400$ and $r = 3$ do not appear in the plot, since the model’s kinetic energy diverges. Also, although the $\text{rMSE}_{\text{test}}$ s of SR-ROM and NN-ROM are similar for $\text{Re} = 500$ (Table 1), SR-ROM has an order of magnitude fewer parameters. Overall, the SR-ROM is the best model in terms of complexity and accuracy.

Finally, the structure of the closure components g_i obtained using symbolic regression for both Reynolds numbers is analyzed in Figure 4.4. Specifically, we count the mean occurrences of the ROM coefficients, and square, trigonometric, and exponential functions over 50 independent runs after simplifying the symbolic expressions. To clarify our definition of “occurrences”, let us consider the expression of the function g_1 for $\text{Re} = 500$, as shown in Table 3,

$$g_1(u_1, u_2, u_3, u_4, u_5) := 0.015u_1 + 0.01u_4 + 1.0 \sin(0.191u_1 - 0.1u_5 + \sin(0.064u_4) - 1.57) + 0.98. \quad (4.7)$$

In the function g_1 , there are two u_1 , two u_4 , one u_5 , and two sine occurrences. The same rule is applied to all the components for each run, and we compute the mean and standard deviation (std) with respect to the number of runs. From Fig. 4.4, we can observe that:

- The logarithm and square are absent from almost all the expressions, thus suggesting that the (general) primitive set that we chose for SR could be reduced without loss in accuracy of the models;
- Except for $r = 5$, the first ROM coefficients u_1 and u_2 appear more frequently than the others (even though their frequency has a significant standard deviation). Intuitively, this could be related to the higher importance of the first modes in the reconstruction of the solution;

- For $r = 5$, the mean occurrences of all the considered terms are much more spread than the previous r values.

We note that the expressions of g_i found via SR do not show any common structure across the two values of Reynolds number. This is possibly a consequence of the training procedure, which was performed by including only data corresponding to a single Reynolds number.

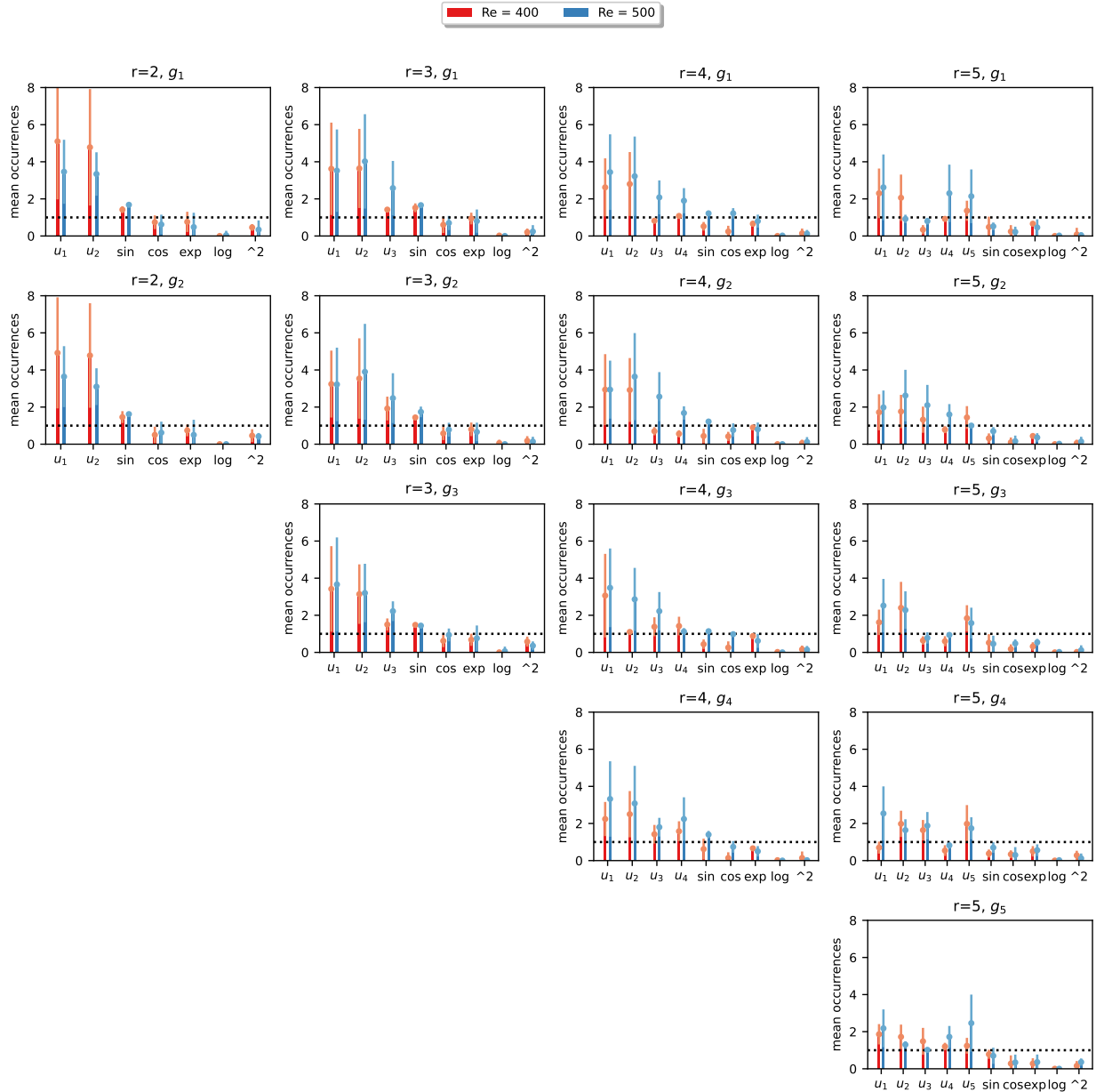


Figure 4.4: 2D flow past a cylinder. Statistics of the occurrences (over 50 independent runs) of the ROM coefficients and primitives appearing in the function g_i found using symbolic regression.

4.2 2D Lid-Driven Cavity

Our next example is the 2D lid-driven cavity (LDC) problem, which is a more challenging test problem compared to the 2D flow past a cylinder. As demonstrated in [5], the problem requires more than 60 POD modes for G-ROM to accurately reconstruct the solutions and quantities of interest. A detailed description of the FOM setup for this problem can be found in [7]. We consider three Reynolds numbers, namely, $Re = 10000$, $Re = 15000$, and $Re = 20000$. The

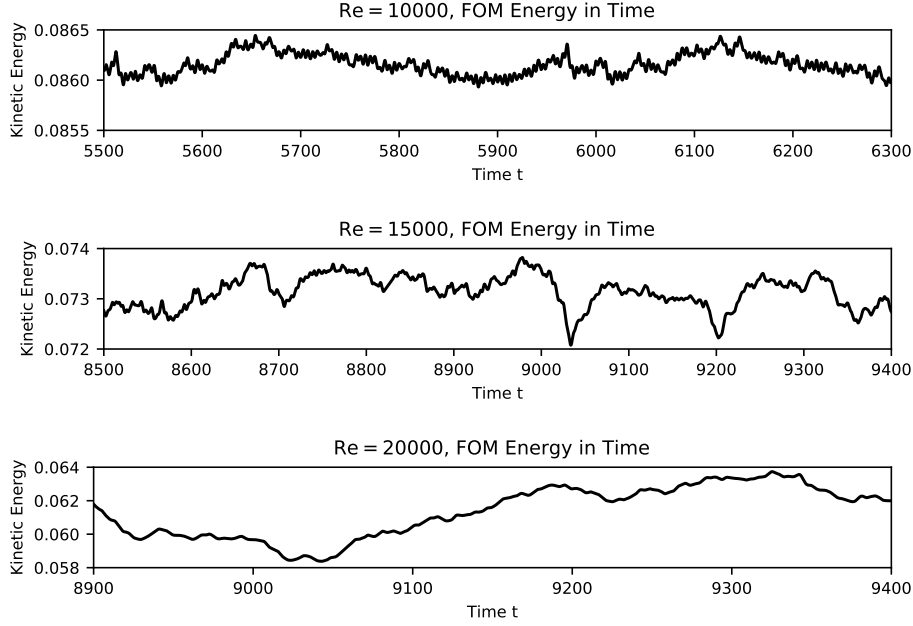


Figure 4.5: 2D lid-driven cavity. The FOM kinetic energy as a function of time t for $Re = 10000, 15000, 20000$.

time evolution of the FOM kinetic energy for the three Reynolds numbers is shown in Fig. 4.5. The results indicate that the solutions at these Reynolds numbers are chaotic.

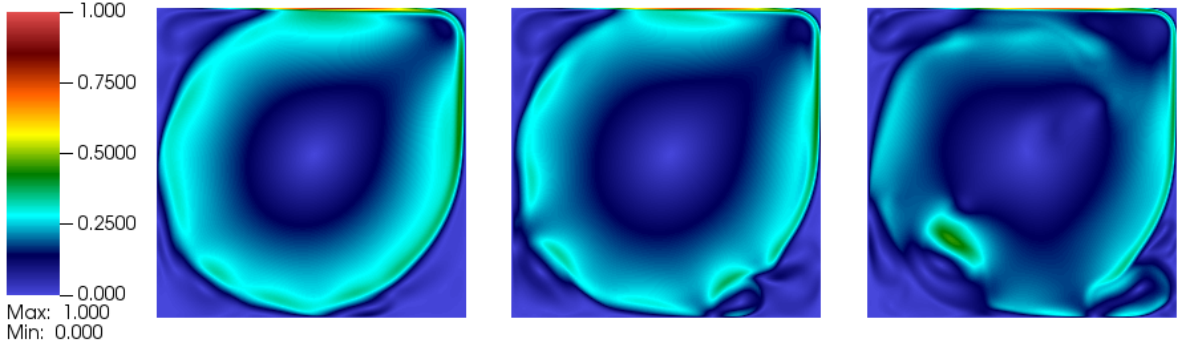


Figure 4.6: 2D lid-driven cavity. The velocity magnitude snapshot for $Re = 10000, 15000, 20000$.

For each Re , $K = 2001$ snapshots $\{\mathbf{u}^k := \mathbf{u}(\mathbf{x}, t^k) - \varphi_0\}_{k=1}^K$ are collected in the time interval $[T_0, T_0 + 80]$ with sampling time step $\Delta t_s = 0.04$, and the zeroth mode, φ_0 , is set to be the FOM velocity field at $t = T_0$. We note that the time T_0 depends on the Reynolds number and is determined such that the solutions are in the statistically steady state region. Snapshots of the velocity magnitude for each considered Re are shown in Fig. 4.6. The snapshot data are then used to construct the reduced basis functions $\{\varphi_i\}_{i=1}^r$ by leveraging POD, the VMS-ROM closure matrix \mathcal{T} , and (3.16). The data-driven closure of each model is trained in the time interval $[T_0, T_0 + 80]$ by minimizing (3.15), and is selected based on the optimal hyperparameters that minimize (4.2) in the time interval $[T_0 + 80, T_0 + 160]$. Finally, we assess the generalization capabilities of all the ROMs in the extrapolation region, that is, in the time interval $[T_0, T_0 + 400]$.

Table 4: 2D lid-driven cavity. Relative MSE ($\text{rMSE}_{\text{test}}$) between the FOM kinetic energy and the predicted kinetic energy in the testing region for all models and reduced space dimension $r = 2, 3, 4, 5, 6, 7$. For the SR-ROM and the NN-ROM, the mean and the standard deviation over 5 independent runs (different seeds) are reported. In bold, the best performing model for each case is listed.

Re	r	LR-ROM	d2-VMS-ROM	SR-ROM	NN-ROM
10000	2	2.8×10^{-5}	2.8×10^{-5}	$(2.8 \pm 0.0) \times 10^{-5}$	$(\mathbf{4.1 \pm 4.2}) \times 10^{-6}$
	3	0.2	2.8×10^{-3}	$(2.2 \pm 2.2) \times 10^{-5}$	$(\mathbf{2.9 \pm 1.3}) \times 10^{-6}$
	4	2.2	0.7	$(\mathbf{4.9 \pm 1}) \times 10^{-6}$	$(\mathbf{5.0 \pm 3.3}) \times 10^{-6}$
	5	1.5×10^{-3}	1.5×10^{-3}	$(\mathbf{4.2 \pm 5.2}) \times 10^{-5}$	$(5.4 \pm 1.5) \times 10^{-3}$
	6	3.1×10^2	7	$(\mathbf{1.5 \pm 1.3}) \times 10^{-5}$	$(2.7 \pm 5.5) \times 10^2$
	7	$\mathbf{2.3 \times 10^{-5}}$	$\mathbf{2.5 \times 10^{-5}}$	$(\mathbf{2.9 \pm 0.2}) \times 10^{-5}$	$(\mathbf{1.9 \pm 3.1}) \times 10^{-5}$
	15000	2	1.4×10^{-4}	$\mathbf{8.4 \times 10^{-5}}$	$(2.8 \pm 0.6) \times 10^{-4}$
3		5.1×10^{-3}	1.8×10^{-4}	$(\mathbf{3.9 \pm 0.5}) \times 10^{-5}$	$(0.6 \pm 1.2) \times 10^6$
4		4×10^{-4}	1.6×10^{-4}	$(\mathbf{8.8 \pm 1.5}) \times 10^{-5}$	$(\mathbf{1.0 \pm 0.4}) \times 10^{-4}$
5		1.9×10^{-4}	$\mathbf{9.2 \times 10^{-5}}$	0.01 ± 0.01	$(\mathbf{7.2 \pm 3.8}) \times 10^{-5}$
6		0.06	1.4×10^{-4}	$(\mathbf{4.8 \pm 0.8}) \times 10^{-5}$	$(6.6 \pm 10) \times 10^{-4}$
7		0.12	1.7×10^{-4}	$(\mathbf{8.2 \pm 3.3}) \times 10^{-5}$	0.04 ± 0.07
20000		2	1.5×10^{-3}	1.1×10^{-3}	$(\mathbf{2.2 \pm 0.6}) \times 10^{-4}$
	3	$\mathbf{1.1 \times 10^{-4}}$	6.3×10^{-4}	$(1.7 \pm 0.4) \times 10^{-4}$	$(5.1 \pm 6.3) \times 10^{-4}$
	4	0.3	6.2×10^{-4}	$(\mathbf{1.8 \pm 0.4}) \times 10^{-4}$	0.7 ± 0.7
	5	2.6×10^{-2}	$\mathbf{3.6 \times 10^{-3}}$	$(\mathbf{3.3 \pm 6.2}) \times 10^{-3}$	$(3.8 \pm 5.2) \times 10^{-2}$
	6	$\mathbf{8.1 \times 10^{-4}}$	2.9×10^{-3}	nan	$(\mathbf{1.8 \pm 1.3}) \times 10^{-3}$
	7	$\mathbf{2 \times 10^{-4}}$	8.6×10^{-4}	$(\mathbf{3.4 \pm 2.6}) \times 10^{-4}$	0.1 ± 0.2

In Table 4, the $\text{rMSE}_{\text{test}}$ between the FOM kinetic energy and the predicted kinetic energy in the extrapolation region of all models is reported with respect to reduced space dimension $r = 2, 3, 4, 5, 6, 7$. The rMSE of the SR-ROM and the NN-ROM is computed by taking the mean of 5 runs with 5 different seeds because these models rely on stochastic optimization algorithms. Similar to the 2D flow past a cylinder case, the results show that the SR-ROM is the most robust model, followed by the NN-ROM, d2-VMS-ROM, and LR-ROM. In particular, we note that for $\text{Re} = 10000$ and $r = 5, 6$, $\text{Re} = 15000$ and $r = 3, 6, 7$, and $\text{Re} = 20000$ and $r = 2$, the SR-ROM $\text{rMSE}_{\text{test}}$ in the extrapolation region is orders of magnitude lower than the $\text{rMSE}_{\text{test}}$ of the other ROMs.

We further measure the closeness between the VMS-ROM closure matrix \mathcal{T} and the reconstructed closure for each model by computing the mean MSE (4.6), see Table 5. We observe that the SR-ROM is the most robust method also in this case. Furthermore, we note that, unlike in the MSE of predicted energy (Table 4), the NN-ROM has a much larger MSE than the SR-ROM. We stress again that this phenomenon is a consequence of the L^2 regularization, which is not used for the SR-ROM.

Similarly to Section 4.1, we report in Table 6 the best symbolic expressions found for the three Reynolds numbers considered. These expressions are slightly more complicated than the ones in Table 3, but this is due to the chaotic, thus more complex, nature of the problem. Also, we remark that for $\text{Re} = 15000$ and 20000 , the best models found depend only polynomially on the FOM coefficients u_r . Hence, also the d2-VMS-ROM could, in principle, find the same models. However, with respect to the $\text{rMSE}_{\text{test}}$ in the extrapolation region, a worse model is found, and this is due to the ill-conditioned linear system to be solved to train this method [12].

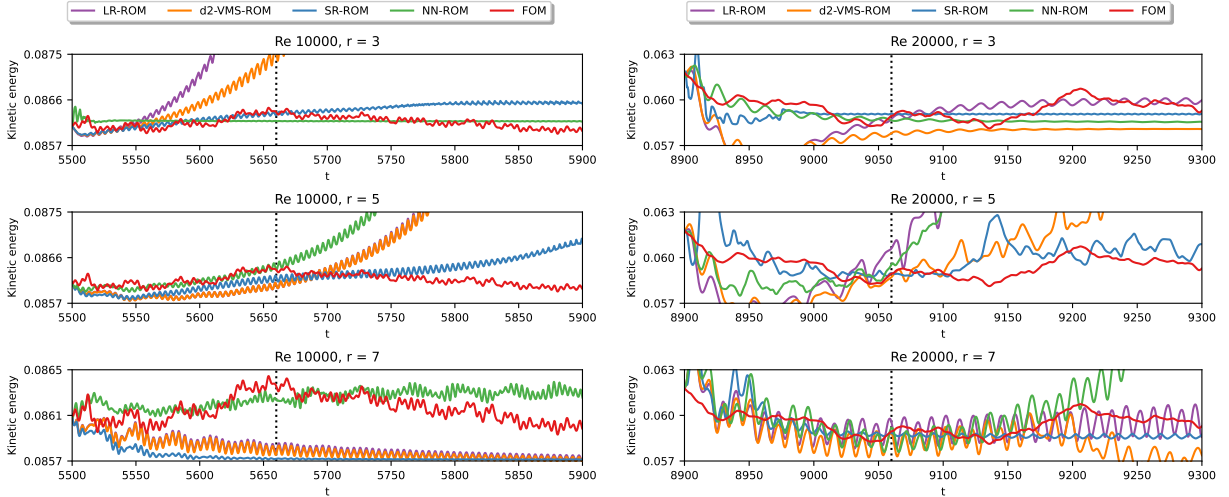
Figure 4.8 confirms, also in this case, that the SR-ROM is the best trade-off between generalization capability ($\text{rMSE}_{\text{test}}$) and model complexity. Again, the SR-ROM and NN-ROM manifest a similar behavior in terms of $\text{rMSE}_{\text{test}}$, especially for $\text{Re} = 10000$ and 15000 , but the SR-ROM has an order of magnitude fewer parameters. Also, the SR-ROM results for $\text{Re} = 20000$ and $r = 6$ are not shown in the figure, since the kinetic energy of one of the SR-ROM best models diverges.

As in Section 4.1, we compute the mean occurrences of some terms using the same strategy. Also in this case, we can make a qualitative analysis:

- The logarithm and square are basically absent for every r and Re ;

Table 5: 2D lid-driven cavity. Mean squared error ($\overline{\text{MSE}}_{\text{tr}}$) between the VMS-ROM closure and the ML-VMS-ROM reconstructed closures for $\text{Re} = 10000, 15000, 20000$. In bold, the best performing model for each case is listed.

Re	r	LR-ROM	d2-VMS-ROM	SR-ROM	NN-ROM
10000	2	2.0×10^{-7}	2.0×10^{-7}	$(1.0 \pm 0.0) \times 10^{-7}$	$(8.9 \pm 3.7) \times 10^{-4}$
	3	1.4×10^{-7}	1.2×10^{-7}	$(9.4 \pm 0.5) \times 10^{-8}$	$(3.3 \pm 2.1) \times 10^{-4}$
	4	1.2×10^{-7}	1.4×10^{-7}	$(7.2 \pm 0.8) \times 10^{-8}$	$(4.7 \pm 2.6) \times 10^{-4}$
	5	1.3×10^{-7}	1.3×10^{-7}	$(6.4 \pm 0.8) \times 10^{-8}$	$(2.4 \pm 0.9) \times 10^{-7}$
	6	9.4×10^{-8}	9.3×10^{-8}	$(5.8 \pm 0.6) \times 10^{-8}$	$(1.9 \pm 1.3) \times 10^{-4}$
	7	1.0×10^{-7}	1.0×10^{-7}	$(5.2 \pm 0.7) \times 10^{-8}$	$(1.2 \pm 1.2) \times 10^{-5}$
	15000	2	1.3×10^{-5}	1.4×10^{-5}	$(6.6 \pm 1.8) \times 10^{-6}$
3		7.9×10^{-6}	4.5×10^{-6}	$(3.5 \pm 0.0) \times 10^{-6}$	$(1.9 \pm 2.5) \times 10^{-4}$
4		5.3×10^{-6}	3.1×10^{-6}	$(2.9 \pm 0.4) \times 10^{-7}$	$(0.1 \pm 2.2) \times 10^{-3}$
5		4.0×10^{-6}	2.3×10^{-6}	$(2.3 \pm 0.4) \times 10^{-6}$	$(9.7 \pm 7.1) \times 10^{-6}$
6		3.6×10^{-6}	2.1×10^{-6}	$(2 \pm 0.4) \times 10^{-6}$	$(8.7 \pm 3.8) \times 10^{-6}$
7		2.7×10^{-6}	2.5×10^{-6}	$(1.7 \pm 1.9) \times 10^{-6}$	$(1.1 \pm 0.5) \times 10^{-5}$
20000		2	9.0×10^{-6}	9×10^{-6}	$(5.4 \pm 0.6) \times 10^{-6}$
	3	9.2×10^{-6}	8.7×10^{-6}	$(4.7 \pm 1.2) \times 10^{-6}$	$(4.2 \pm 5.5) \times 10^{-6}$
	4	1.1×10^{-5}	9.3×10^{-6}	$(4.3 \pm 0.5) \times 10^{-6}$	$(1.1 \pm 0.1) \times 10^{-5}$
	5	9.8×10^{-6}	1.0×10^{-5}	$(6.5 \pm 0.9) \times 10^{-6}$	$(3.2 \pm 4) \times 10^{-5}$
	6	7.4×10^{-6}	7.6×10^{-6}	$(4.9 \pm 0.5) \times 10^{-6}$	$(1.0 \pm 1.8) \times 10^{-4}$
	7	7.3×10^{-6}	7.6×10^{-6}	$(5.3 \pm 0.8) \times 10^{-6}$	$(7.6 \pm 0.1) \times 10^{-6}$


 Figure 4.7: 2D lid-driven cavity at $\text{Re} = 10000$ and $\text{Re} = 20000$. Comparison of the kinetic energy between the FOM and the ROMs with $r = 3, 5, 7$.

- For $r = 5, 6, 7$ and for each Reynolds number, the mean occurrence of every term is uniform, *i.e.*, none of the terms in the expressions is dominant.

As in Section 4.1, no evident structure emerges in the expressions of Table 6 across different values of the Reynolds number because the training procedure of all the ROMs is carried out at a fixed Reynolds number.

In Figure 4.7, we show the kinetic energy as a function of time for the ROMs and the FOM with reduced space dimension $r = 3, 5, 7$, for $\text{Re} = 10000$ and $\text{Re} = 20000$. For $\text{Re} = 10000$, the SR-ROM outperforms the other ROMs for $r = 5$, while for $r = 3, 7$ the SR-ROM is still among the best performing models. We observe that the d2-VMS-ROM and LR-ROM deviate in the extrapolation region for $r = 3, 5$, as does the NN-ROM for $r = 5$. The

Table 6: 2D lid driven cavity. Expressions of the components of the SR-ROM closure model that attains the minimum $\text{rMSE}_{\text{test}}$ in the extrapolation region among those reported in Table 4.

Re	Component	Expression
10000	g_1	$0.0002u_1 + 0.0901u_2 + 0.0003u_3 - 0.0004u_4 + (0.0001u_1 - 0.0001u_2)*$ $* \cos(3.7331u_4 - 2.1130) + (0.0002u_1 + 0.0010u_2 + 0.0005u_3 - 0.0007u_4 + 0.0004)*$ $* \sin(0.0686u_1 - \cos(0.6297u_1 - 0.1635u_3)) - 0.999 \sin(0.0897u_2) + 0.0003$
	g_2	$-0.0003u_1 + 0.0003u_2 + 0.0002u_3 - \sin((0.0883u_2(1.7855u_1 + 1.8087u_2) -$ $-\sin(1.2270u_2 + 0.5128u_4 - 7.0881) + 0.9256) \sin(\sin(\sin(0.0006u_3) - 0.0009))*$ $* \sin(\sin(\sin(\sin(0.8346u_1)) + \cos(0.7177u_1 + 0.9317)))) - 0.0004$
	g_3	$0.0001u_2 + 0.0001u_3 + (0.0005u_1u_3 - 0.0003u_2 - 0.0003u_4)(0.4274u_1 - 0.1150u_4 +$ $+(0.0507u_1 - 0.0376u_2 \cos(1.1193u_2) + 0.0342u_3)(1.6577u_1 + 0.5313u_2 - 7.1728) +$ $+ \sin(0.7269u_2 + 1.0911u_3 + 0.5615) \cos(0.6477u_1))$
	g_4	$1.0010 \sin(0.0299u_2 + 0.0659u_4 + (0.3499u_1 - \cos(1.6868u_1))(0.4145u_4 + \sin((0.4721u_2 -$ $-\sin(0.7269u_3)) \cos(0.6962u_1) + 2.7152)0.0006 - \sin(0.0301u_2 + 0.0659u_4))$
15000	g_1	$-0.0022 - 0.0006u_1 + 0.0004u_0^2(1.9712 + 0.5332u_0) - 0.0001u_1u_0 -$ $-(-0.0004 - 0.0001u_1)(0.7896u_2 + 2.7564u_1^2)$
	g_2	$0.0001 + 0.9990(20.9826 + 9.6691u_0 + 7.9730u_2 + (1.1479 + 0.0092u_0(-22.8110u_0$ $+ 27.8969u_1 + 9.8753u_2) - 3.1177u_1(0.1684 + 0.0210u_2))(-13.6013 - 8.9292u_1 +$ $+ (-2.5189 + 0.2241u_0 - 1.2826u_2)(6.0625 + 2.3368u_0 + 1.1539u_1 - 0.0070u_2)))$ $(-0.0002 + 0.0001u_1 + 0.0002u_2)$
	g_3	$0.0038 - 0.0006u_0 - 0.0019u_2 + 0.0001u_2u_0 + (0.0010 - 0.0007u_2)(-2.4952 +$ $+ 0.0602u_1 + 0.1949u_2 + (0.2424u_1 + 0.1948u_2u_1)(1.1255u_0 - 1.2423u_1 + 2.9477u_2))$
20000	g_1	$0.0002u_1 + 0.0008u_2 - 0.0005u_3 + (6.0344u_2 - 4.848u_4)(0.0001u_1(1.9919u_1u_3*$ $*(3.2164u_1 + 1.9255u_4 - 3.5296) - 4.4491u_2 - 2.9491u_3 + 8.9232)) - 0.0004$
	g_2	$1.0021(0.3193u_2(0.7430u_1 + 1.8020u_4)(0.1953u_2 - 1.4475)(5.9033u_2 + 10.0442) +$ $+ 12.5300u_4 - (0.5016u_2 - 4.5800u_3)(1.1975u_2 + 2.6217)(0.3743u_3 - 0.0664))*$ $*(0.0002u_1 + 0.0001u_2) - 0.0001$
	g_3	$0.0003u_3 - 0.0002u_4 + (0.0001u_2 - 0.0001u_3)(1.7047u_2^2 + 2.8970u_4 - 0.9176)(13.6070u_1 -$ $- 1.5597u_3 + 5.6265u_4 - 6.6889) - (0.0021u_2 + 0.0011u_4)(1.5428u_2 - 0.6498u_3) + 0.002$
	g_4	$-0.9953(0.0001u_2 + 0.0001u_3^2 - 0.0001u_3 + 0.001u_4 - (0.0001u_1 + 0.0010)*$ $*(1.2730u_4 + 0.300))(4.1908u_2^2 + 9.7453u_2 - 0.1684u_3(70.4595u_1 +$ $+ 13.7008) + 4.0931u_4 + 3.2191)$

SR-ROM is the only method that remains close to the FOM in this case. Finally, for $\text{Re} = 20000$, the SR-ROM is the best method for $r = 3, 5, 7$.

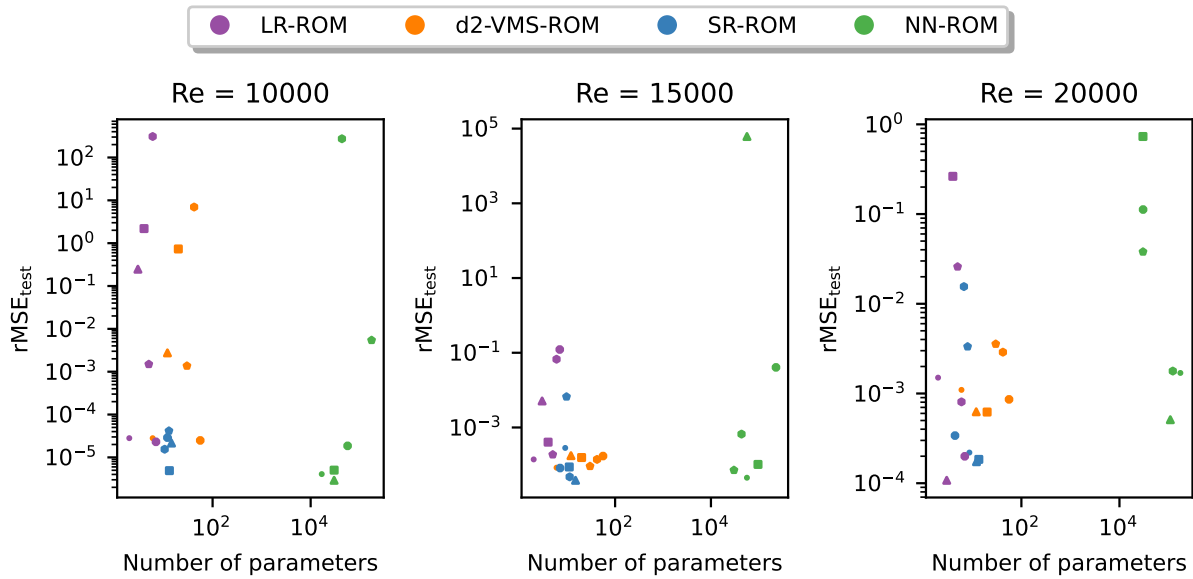


Figure 4.8: 2D lid-driven cavity. $rMSE_{test}$ as a function of the number of parameters of the model. For the SR-ROM and NN-ROM, the mean values over 5 independent runs are reported. Each point is marked using the following legend: point for $r = 2$; triangle for $r = 3$; square for $r = 4$; pentagon for $r = 5$; hexagon for $r = 6$; octagon for $r = 7$.

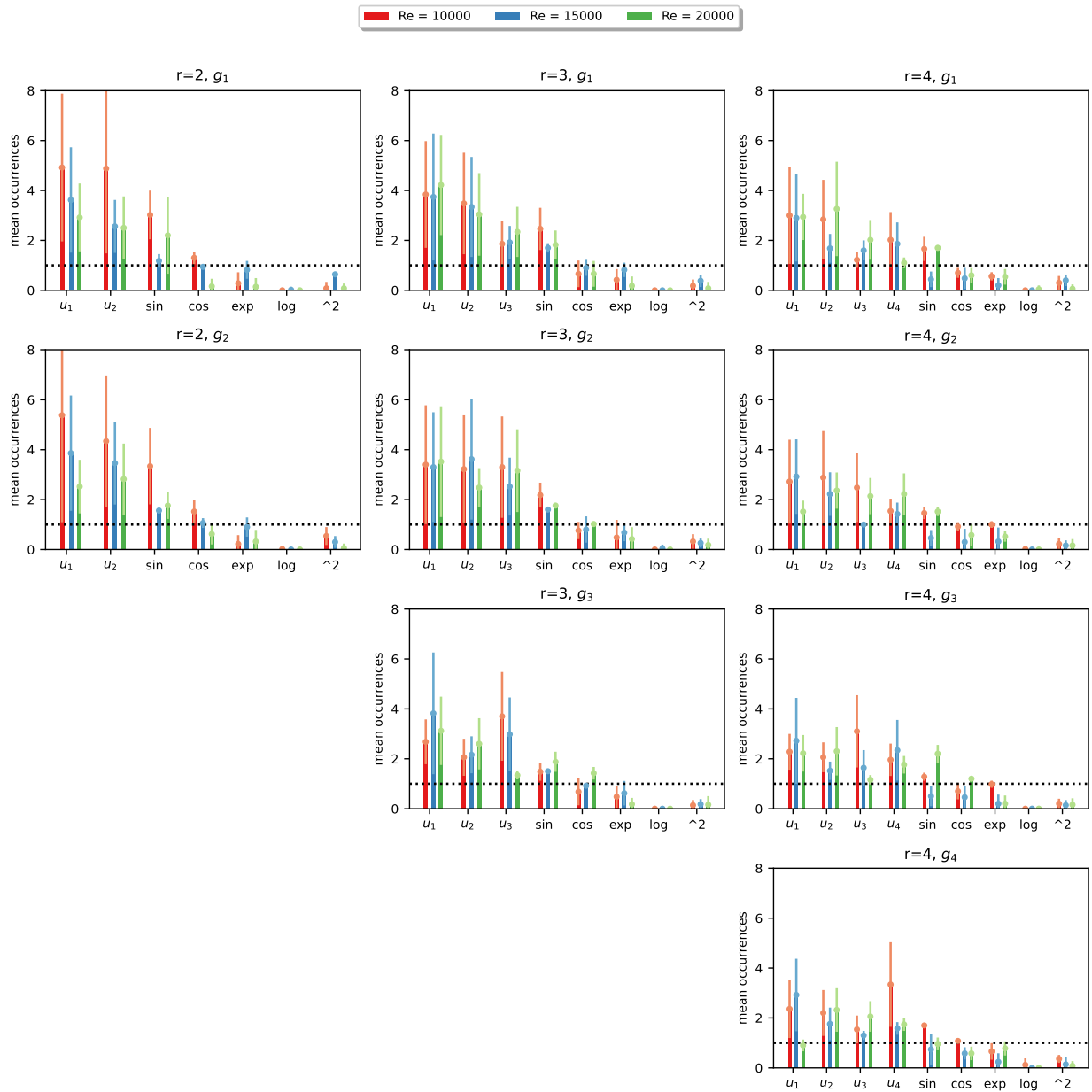


Figure 4.9: 2D lid-driven cavity, $r = 2, 3, 4$. Statistics of the occurrences (over 50 independent runs) of the ROM coefficients and primitives appearing in the closure model found by SR-ROM.

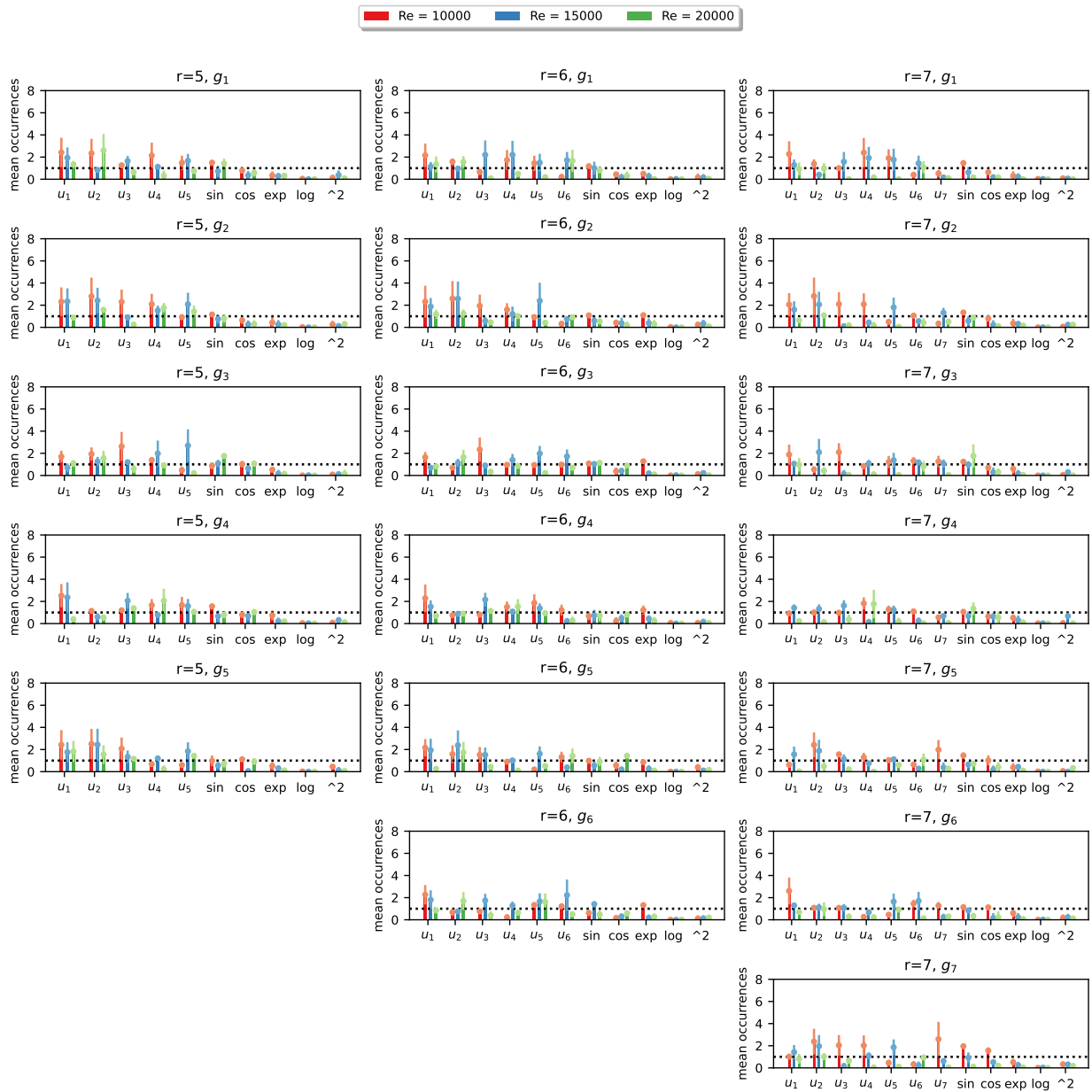


Figure 4.10: 2D lid-driven cavity, $r = 5, 6, 7$. Statistics of the occurrences (over 50 independent runs) of the ROM coefficients and primitives in the closure model found by SR-ROM.

5 Conclusions and Future Work

In this paper, we propose a novel symbolic regression (SR) closure strategy for ROM, which leverages available data and SR to find the ROM closure model. The new SR-ROM closure model combines the advantages of current data-driven ROM closure approaches and eliminates their drawbacks: The new data-driven SR closures yield ROMs that are interpretable, parsimonious, accurate, generalizable, and robust. To compare the SR-ROM closures with the current data-driven ROM closures (i.e., structural and machine learning ROM closures), we consider a specific ROM closure framework, the data-driven variational multiscale ROM. Within this framework, we compare the novel SR-ROM closure with three other data-driven ROM closures: a linear regression ROM closure, a quadratic data-driven ROM closure, and a neural network ROM closure. To investigate the four types of ROM closures, we consider two under-resolved, convection-dominated test problems: the flow past a cylinder and the lid-driven cavity flow. To assess the performance of the different types of closures, we monitor the performance of the ROMs obtained by adding the four ROM closure models.

Our numerical investigation yields the following conclusions:

- For both test problems, in the predictive regime, the new SR-ROM closure yields more accurate results than the other three ROM closures (i.e., the linear regression, quadratic data-driven, and neural network ROM closures);
- The SR-ROM is the most robust model with respect to the ROM space dimension, r ;
- Our numerical results also show that the new SR-ROM closure has orders of magnitude fewer terms than the neural network closure model;
- The SR strategy is more accurate than the other three data-driven approaches in reconstructing the ROM closure term.

The first steps in the numerical investigation of the new SR-ROM have been encouraging. There are, however, several other research directions that should be pursued next. For example, in this paper, we did not find common structures in the SR-ROM closures for different Reynolds numbers. This is because we used training data for a fixed Reynolds number. To allow SR to discover common structures in the new SR-ROM closures, we plan to train it with data from different Reynolds numbers. We also note that, although the SR-ROM is used in this paper for prediction in time, the Reynolds number is fixed. We plan to extend the new SR-ROM to parametric problems, and use it to predict solutions and quantities of interests at other Reynolds numbers. Another interesting research direction is the investigation of the new SR-ROM strategy in ROM closure frameworks that are different from the variational multiscale ROM closure approach considered in this paper. For example, we plan to investigate the new SR-ROM closure for large eddy simulation ROMs constructed by using ROM spatial filtering [12]. Finally, we plan to compare the new SR-ROM closure strategy with other data-driven modeling approaches, e.g., operator inference [31, 41], SINDy [42, 43], and LaSDI [44].

6 CRediT Authorship Contribution Statement

Simone Manti: Writing - original draft, Writing - review and editing, Data curation, Investigation, Conceptualization, Validation, Visualization, Methodology, Software. **Ping-Hsuan Tsai:** Writing - original draft, Writing - review and editing, Data curation, Investigation, Conceptualization, Validation, Visualization, Methodology, Software. **Alessandro Lucantonio:** Writing - review and editing, Conceptualization, Validation, Methodology, Resources, Funding acquisition, Supervision. **Traian Iliescu:** Writing - original draft, Writing - review and editing, Conceptualization, Validation, Methodology, Funding acquisition, Supervision.

Acknowledgments

The work of SM and AL is supported by the European Union (European Research Council (ERC), ALPS, 101039481). Views and opinions expressed are however those of the author(s) only and do not necessarily reflect those of the European Union or the ERC Executive Agency. Neither the European Union nor the granting authority can be held responsible for them. Computational resources have been partially provided by DeiC National HPC (DeiC-AU-N1-2023030). TI acknowledges support through National Science Foundation grants DMS-2012253 and CDS&E-MSS-1953113.

References

- [1] J. S. Hesthaven, G. Rozza, and B. Stamm. *Certified Reduced Basis Methods for Parametrized Partial Differential Equations*. Springer, 2015.
- [2] A. Quarteroni, A. Manzoni, and F. Negri. *Reduced Basis Methods for Partial Differential Equations: An Introduction*, volume 92. Springer, 2015.
- [3] P.T. Tsai, P. Fischer, and E. Solomonik. Accelerating the Galerkin reduced-order model with the tensor decomposition for turbulent flows. *arXiv preprint*, <http://arxiv.org/abs/2311.03694>, 2023.
- [4] S. E. Ahmed, S. Pawar, O. San, A. Rasheed, T. Iliescu, and B. R. Noack. On closures for reduced order models – A spectrum of first-principle to machine-learned avenues. *Phys. Fluids*, 33(9):091301, 2021.
- [5] L. Fick, Y. Maday, A. T. Patera, and T. Taddei. A stabilized POD model for turbulent flows over a range of Reynolds numbers: Optimal parameter sampling and constrained projection. *J. Comp. Phys.*, 371:214–243, 2018.
- [6] K. Kaneko. *An augmented basis method for reduced order models of turbulent flow*. PhD thesis, 2022.
- [7] K. Kaneko, P.-H. Tsai, and P. Fischer. Towards model order reduction for fluid-thermal analysis. *Nucl. Eng. Des.*, 370:110866, 2020.
- [8] E. J. Parish, M. Yano, I. Tezaur, and T. Iliescu. Residual-based stabilized reduced-order models of the transient convection-diffusion-reaction equation obtained through discrete and continuous projection. *Arch. Comput. Methods Eng.*, pages 1–45, 2024.
- [9] P.H. Tsai, P. Fischer, and T. Iliescu. A time-relaxation reduced order model for the turbulent channel flow. *J. Comput. Phys.*, page 113563, 2024.
- [10] B. Sanderse, P. Stinis, R. Maulik, and S. E. Ahmed. Scientific machine learning for closure models in multiscale problems: A review. *arXiv preprint arXiv:2403.02913*, 2024.
- [11] C. Mou, B. Koc, O. San, L. G. Rebholz, and T. Iliescu. Data-driven variational multiscale reduced order models. *Comput. Methods Appl. Mech. Engrg.*, 373:113470, 2021.
- [12] X. Xie, M. Mohebujaman, L. G. Rebholz, and T. Iliescu. Data-driven filtered reduced order modeling of fluid flows. *SIAM J. Sci. Comput.*, 40(3):B834–B857, 2018.
- [13] S. E. Ahmed, O. San, A. Rasheed, T. Iliescu, and A. Veneziani. Physics guided machine learning for variational multiscale reduced order modeling. *SIAM J. Sci. Comput.*, 45(3):B283–B313, 2023.
- [14] X. Xie, C. Webster, and T. Iliescu. Closure learning for nonlinear model reduction using deep residual neural network. *Fluids*, 5(1):39, 2020.
- [15] C. Mou, Z. Wang, D. R. Wells, X. Xie, and T. Iliescu. Reduced order models for the quasi-geostrophic equations: A brief survey. *Fluids*, 6(1):16, 2021.
- [16] T. J. R. Hughes. Multiscale phenomena: Green’s functions, the Dirichlet-to-Neumann formulation, subgrid scale models, bubbles and the origins of stabilized methods. *Comput. Methods Appl. Mech. Engrg.*, 127(1-4):387–401, 1995.
- [17] Y. Maday, A. T. Patera, and E. M. Ronquist. A well-posed optimal spectral element approximation for the Stokes problem. Technical report, 1987.
- [18] P. Fischer, M. Schmitt, and A. Tomboulides. Recent developments in spectral element simulations of moving-domain problems. In *Recent Progress and Modern Challenges in Applied Mathematics, Modeling and Computational Science*, pages 213–244. Springer, 2017.
- [19] P.T. Tsai and P. Fischer. Parametric model-order-reduction development for unsteady convection. *Front. Phys.*, 10:903169, 2022.
- [20] G. Berkooz, P. Holmes, and J. L. Lumley. The proper orthogonal decomposition in the analysis of turbulent flows. *Ann. Rev. Fluid Mech.*, 25(1):539–575, 1993.
- [21] S. Volkwein. Proper Orthogonal Decomposition: Theory and Reduced-Order Modelling. *Lecture Notes, University of Konstanz*, 2013. <http://www.math.uni-konstanz.de/numerik/personen/volkwein/teaching/POD-Book.pdf>.
- [22] F. Ballarin, A. Manzoni, A. Quarteroni, and G. Rozza. Supremizer stabilization of POD–Galerkin approximation of parametrized steady incompressible Navier–Stokes equations. *Int. J. Numer. Meth. Engrg.*, 102:1136–1161, 2015.

- [23] V. DeCaria, T. Iliescu, W. Layton, M. McLaughlin, and M. Schneier. An artificial compression reduced order model. *SIAM J. Numer. Anal.*, 58(1):565–589, 2020.
- [24] B. R. Noack, P. Papas, and P. A. Monkewitz. The need for a pressure-term representation in empirical Galerkin models of incompressible shear flows. *J. Fluid Mech.*, 523:339–365, 2005.
- [25] T. J. R. Hughes, G. R. Fejjoó, L. Mazzei, and J.-B. Quincy. The variational multiscale method – a paradigm for computational mechanics. *Comput. Methods Appl. Mech. Engrg.*, 166(1):3–24, 1998.
- [26] N. Ahmed, T. C. Rebollo, V. John, and S. Rubino. A review of variational multiscale methods for the simulation of turbulent incompressible flows. *Arch. Comput. Method. E.*, 24(1):115–164, 2017.
- [27] R. Codina, S. Badia, J. Baiges, and J. Principe. Variational multiscale methods in computational fluid dynamics. *Encyclopedia of Computational Mechanics Second Edition*, pages 1–28, 2018.
- [28] B. Koc, M. Mohebujaman, C. Mou, and T. Iliescu. Commutation error in reduced order modeling of fluid flows. *Adv. Comput. Math.*, 45(5-6):2587–2621, 2019.
- [29] H. Trevor, T. Robert, and F. Jerome. *The Elements of Statistical Learning: Data Mining, Inference and Prediction*. Springer, 2009.
- [30] J. Gareth, W. Daniela, H. Trevor, and T. Robert. *An Introduction to Statistical Learning: With Applications in R*. Springer, 2021.
- [31] B. Peherstorfer and K. Willcox. Data-driven operator inference for nonintrusive projection-based model reduction. *Comput. Methods Appl. Mech. Engrg.*, 306:196–215, 2016.
- [32] G. Kronberger, B. Burlacu, M. Kommenda, S. M. Winkler, and M. Affenzeller. *Symbolic Regression*. CRC Press, 2024.
- [33] S. Manti and A. Lucantonio. Discovering interpretable physical models using symbolic regression and discrete exterior calculus. *Mach. Learn.: Sci. Technol.*, 5(1):015005, 2024.
- [34] J. R. Koza. *Genetic Programming as a Means for Programming Computers by Natural Selection*, volume 4. Stat. Comput., 1994.
- [35] R. Poli, W.B. Langdon, and N.F. McPhee. *A Field Guide to Genetic Programming*. Lulu Enterprises UK, 2009.
- [36] B. Burlacu, G. Kronberger, and M. Kommenda. Operon C++: An efficient genetic programming framework for symbolic regression. GECCO '20, page 1562–1570, New York, NY, USA, 2020. Association for Computing Machinery.
- [37] W. La Cava, B. Burlacu, M. Virgolin, M. Kommenda, P. Orzechowski, F. O. de França, Y. Jin, and J. H. Moore. Contemporary symbolic regression methods and their relative performance. *NeurIPS*, 2021(DB1):1, 2021.
- [38] D. E. Rumelhart, G. E. Hinton, and R. J. Williams. Learning representations by back-propagating errors. *Nature*, 323(6088):533–536, 1986.
- [39] I. Goodfellow, Y. Bengio, and A. Courville. *Deep Learning*. MIT Press, 2016. <http://www.deeplearningbook.org>.
- [40] M. Tietz, T. J. Fan, D. Nouri, B. Bossan, and Skorch Developers. skorch: A scikit-learn compatible neural network library that wraps pytorch. <https://skorch.readthedocs.io/en/stable>, 2017.
- [41] N. Aretz and K. Willcox. Exploiting structure via nested operator inference in physics-based learning. *MORE 2024*, page 12.
- [42] S. L. Brunton, J. L. Proctor, and J. N. Kutz. Discovering governing equations from data by sparse identification of nonlinear dynamical systems. *Proc. Natl. Acad. Sci.*, 113(15):3932–3937, 2016.
- [43] D. A. Messenger and D. M. Bortz. Weak SINDy for partial differential equations. *J. Comput. Phys.*, 443:110525, 2021.
- [44] W. D. Fries, X. He, and Y. Choi. Lasdi: Parametric latent space dynamics identification. *Comput. Methods Appl. Mech. Engrg.*, 399:115436, 2022.